Storm-Scale Polarimetric Radar Signatures Associated with Tornado Dissipation in Supercells

JACOB H. SEGALL,[a] MICHAEL M. FRENCH,[a] DARREL M. KINGFIELD,[b,c] SCOTT D. LOEFFLER,[d] and MATTHEW R. KUMJIAN[d]

[a] *School of Marine and Atmospheric Sciences, Stony Brook University, State University of New York, Stony Brook, New York*
[b] *Cooperative Institute for Research in Environmental Sciences, University of Colorado Boulder, Boulder, Colorado*
[c] *NOAA/Global Systems Laboratory, Boulder, Colorado*
[d] *Department of Meteorology and Atmospheric Sciences, The Pennsylvania State University, University Park, Pennsylvania*

(Manuscript received 30 April 2021, in final form 15 October 2021)

ABSTRACT: Polarimetric radar data from the WSR-88D network are used to examine the evolution of various polarimetric precursor signatures to tornado dissipation within a sample of 36 supercell storms. These signatures include an increase in bulk hook echo median raindrop size, a decrease in midlevel differential radar reflectivity factor (Z_{DR}) column area, a decrease in the magnitude of the Z_{DR} arc, an increase in the area of low-level large hail, and a decrease in the orientation angle of the vector separating low-level Z_{DR} and specific differential phase (K_{DP}) maxima. Only supercells that produced "long-duration" tornadoes (with at least four consecutive volumes of WSR-88D data) are investigated, so that signatures can be sufficiently tracked in time, and novel algorithms are used to isolate each storm-scale process. During the time leading up to tornado dissipation, we find that hook echo median drop size (D_0) and median Z_{DR} remain relatively constant, but hook echo median K_{DP} and estimated number concentration (N_T) increase. The Z_{DR} arc maximum magnitude and Z_{DR}–K_{DP} separation orientation angles are observed to decrease in most dissipation cases. Neither the area of large hail nor the Z_{DR} column area exhibit strong signals leading up to tornado dissipation. Finally, combinations of storm-scale behaviors and TVS behaviors occur most frequently just prior to tornado dissipation, but also are common 15–20 min prior to dissipation. The results from this study provide evidence that nowcasting tornado dissipation using dual-polarization radar may be possible when combined with TVS monitoring, subject to important caveats.

KEYWORDS: Severe storms; Supercells; Tornadoes; Convective storms; Radars/Radar observations; Nowcasting

1. Background

The societal impact of tornadoes is well understood; they are a severe hazard that poses an immediate threat to human life and typically cause hundreds of millions of dollars in damage to property annually in the United States (Changnon 2009). In recent years, observational and modeling efforts to understand the important processes ongoing within supercell thunderstorms, the storm mode responsible for a large majority of the most violent tornadoes, has provided deeper insight into how tornadoes form (e.g., Wurman et al. 2012; Markowski and Richardson 2014). However, the processes responsible for tornado maintenance and dissipation have been less studied. Additionally, despite recent advances in our understanding of storm- and tornado-scale processes within supercell thunderstorms, a major challenge remains in leveraging such information into accurate and timely short-term forecasting (i.e., "nowcasting") of the tornado life cycle.

Ideally, skillful nowcasting of supercellular tornadoes is achieved by identifying known features or ongoing processes in operational remote sensing data that are thought to indicate that tornado formation or evolution is imminent. Many observational studies have investigated the tornado's life cycle using mobile and airborne radar data with a focus on the tornadogenesis process (e.g., Brandes 1977; Dowell and Bluestein 2002a,b; Bluestein et al. 2003; Wurman et al. 2007; Markowski et al. 2012, 2018; Kosiba et al. 2013; French et al. 2013; Houser et al. 2015), while fewer efforts have examined tornado dissipation (e.g., Marquis et al. 2012). Further, most of the work on tornado dissipation comes from case studies (e.g., French et al. 2014; Houser et al. 2015), which inherently limit our capability to generalize any findings. Only recently, in French and Kingfield (2019, hereafter FK19) were efforts focused on identification of repeatable radar features in dissipating tornadoes. Their study analyzed previously identified behaviors of the tornadic vortex signature (TVS), the small-scale cyclonic shear feature that is the tornado's bulk representation in Doppler velocity data, to determine whether its behaviors were associated with tornado dissipation. FK19 found that three of their identified behaviors (TVS intensity decreases, storm-relative rearward TVS motion, and large horizontal displacement between the TVS and the midlevel updraft) did portend tornado dissipation, and concluded that tornado dissipation may be skillfully predicted using only radar data.

FK19 emphasized that their focus was only on behaviors of the TVS identified from previous case studies, and that other storm-scale radar signatures may be associated with tornado dissipation. Based on the integrative observational and modeling work of Marquis et al. (2012), tornado decay may occur for several different reasons. For example, features like

Segall's current affiliation: CIMMS/OU/NSSL, Norman, Oklahoma.

Corresponding author: Jacob H. Segall, jacob.segall@noaa.gov

DOI: 10.1175/WAF-D-21-0067.1

secondary surges of the rear-flank downdraft and the accompanying gust front, or internal storm conditions like the rear-flank outflow temperature and buoyancy profile near the surface, likely play roles in tornado maintenance. These processes occur on small spatiotemporal scales that are difficult to observe with current real-time operational capabilities, and in situ measurements of thermodynamic, kinematic, and microphysical quantities within supercells are difficult to retrieve owing to the presence of severe hazards within storms, in addition to the scales on which these processes occur. However, the upgrade of the WSR-88D network to dual-polarization capabilities, completed in 2013, is one potential alternative to mitigate such observational difficulties.

Polarimetric radar quantities are sensitive to several characteristics of hydrometeors, including size, shape, liquid water content (LWC), orientation, and heterogeneity in a volume; some of the information derived from polarimetric radar variables can be leveraged to gain insight into dynamic processes, thermodynamic characteristics, and microphysical processes remotely (Kumjian 2013a,b,c). Within supercells, several repeatable polarimetric "signatures" are observed, and each is an indicator of an ongoing storm- or tornado-scale process (Kumjian and Ryzhkov 2008a). In addition, polarimetric radar data can be used to infer information about rain drop size distributions (DSDs) in supercells, which also may provide insight into ongoing microphysical processes (e.g., Kumjian 2011). In turn, some of the processes that produce signatures or indicate DSD changes also may indicate a greater or lesser likelihood of tornado dissipation. Thus, analysis of polarimetric radar data may provide evidence of additional signatures beyond those identified in FK19, that are associated with tornado dissipation.

The ability to skillfully nowcast tornado dissipation would be beneficial to emergency managers and first responders attempting to address the areas impacted by strong and violent tornadic events. In addition, the presence of multiple dissipation behaviors combined with observed tornado dissipation may provide forecasters increased confidence that a tornado will not reform immediately after dissipation, and, therefore, impact subsequent tornado warning decisions resulting in a lower false alarm rate (FAR). *Thus, the goal of this paper is to identify any trends, in a bulk sense, in previously identified storm-scale polarimetric signatures from volume to volume leading up to tornado dissipation. Additionally, relationships between storm-scale polarimetric features and the TVS behaviors identified in FK19 are investigated.* The initial evidence from FK19 that dissipation may be predictable, combined with past case study work establishing that polarimetric features within supercells may also indicate processes unsupportive of tornado maintenance (summarized and justified in section 2), motivates further study of potential tornado dissipation predictors. Section 3 details the dataset, the methods used for identifying and quantifying various polarimetric signatures, and the statistical analysis technique. Section 4 discusses the results from the five polarimetric signatures, while a discussion and summary of findings is presented in section 5. This study is one in an ongoing series of related climatological efforts to investigate polarimetric aspects of supercells (FK19; Loeffler et al. 2020; Tuftedal et al. 2021).

2. Polarimetric radar signatures and behaviors

There are a number of polarimetric signatures and features that could be studied and related to the tornado life cycle. Instead of analyzing all of them and searching for the best statistical matches, we take a hypothesis-driven approach largely driven by past work. Background and explanation for the five behaviors we chose appear in this section.

a. Hook echo raindrop size

The thermodynamic characteristics of the hook echo, forced by various dynamical and microphysical processes, are known to be important to the tornadogenesis process (Markowski et al. 2002; Grzych et al. 2007; Hirth et al. 2008). However, less discussed in the literature is that the character of the RFD outflow also plays an integral role in the *maintenance* of an ongoing tornado (e.g., Marquis et al. 2012). Indeed, Lee et al. (2012) explicitly found colder surface air in the RFD outflow region adjacent to a violent tornado just prior to its dissipation compared to four separate earlier tornado time periods in their observational case study. Thus, quantifying processes that impact the thermodynamic character of the RFD outflow air may prove useful in determining the likelihood of tornado dissipation.

Evaporation is difficult to observe and measure directly in real time, but its effects on DSDs may be quantifiable by utilizing polarimetric radar variables. For example, the differential radar reflectivity factor (Z_{DR}), in pure rain, becomes increasingly positive for larger raindrops and can be used as an estimate of the median raindrop size in a radar volume. Thus, monitoring the evolution in Z_{DR} within the hook echo could provide information about the degree of evaporation occurring within this region. In turn, we may surmise that the greater the evaporation rate, the more cold, negatively buoyant surface air is introduced into a region that contributes parcels to the low-level updraft and tornado, and the greater the likelihood of tornado dissipation. Indeed, Kumjian and Ryzhkov (2008b), Kumjian (2011), and French et al. (2015) all found that tornadic hook echoes were generally associated with DSDs skewed toward smaller drops as compared to nontornadic supercells. However, follow-up work by Tuftedal et al. (2021) found more subtle differences among larger datasets. Nonetheless, French et al. (2015) also monitored the progression of estimated DSDs for three tornado dissipation cases. Specifically, in two cases, *they found hook echo median drop sizes increased prior to tornado dissipation and in a third case, there was no change.* The authors speculated that an observable increase in Z_{DR} within the hook echo due to increasing evaporation rates and more negatively buoyancy profiles may precede tornado dissipation (Fig. 1a).

More recently, McKeown et al. (2020) also found an increase in Z_{DR} both during a rapid decrease in intensity of a violent tornado and several minutes later, just prior to its dissipation. They also found that another polarimetric variable, the specific differential phase (K_{DP}), increased during both periods as well. The K_{DP} is the range derivative of the differential phase shift (Φ_{DP}; see, e.g., Bringi and Chandrasekar 2001; Reimel and Kumjian 2021) and, in pure rain, positive

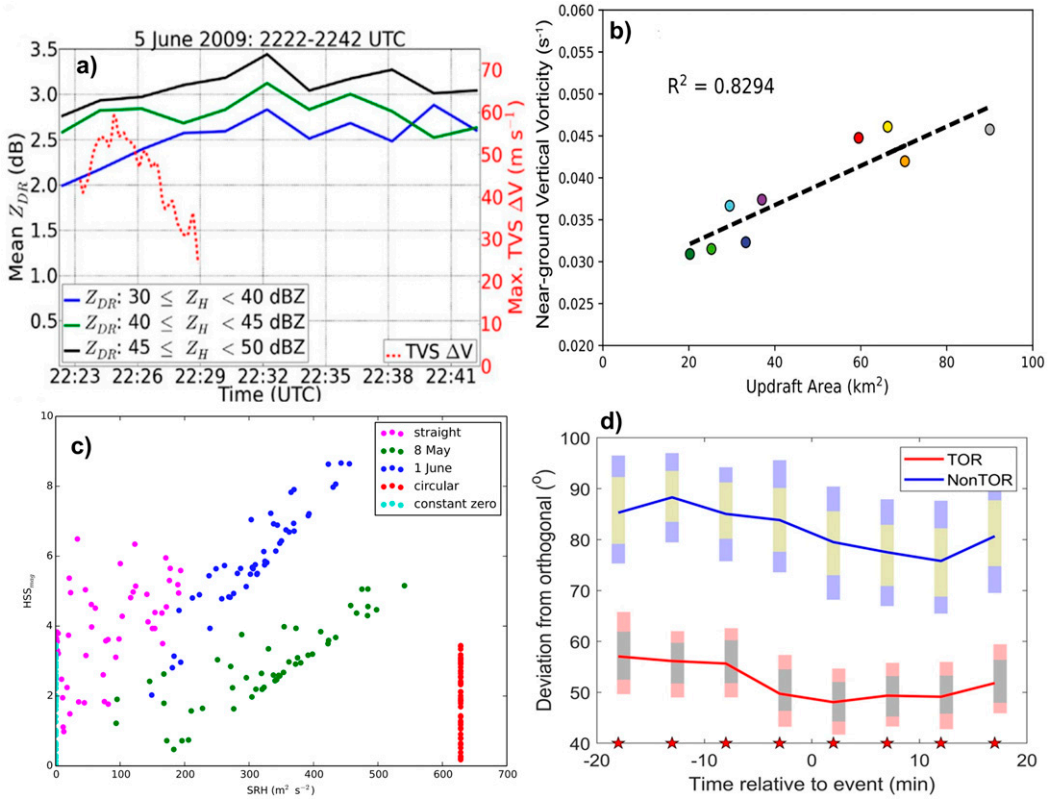

FIG. 1. Evidence from past studies relating storm-scale processes to tornadic environments. (a) From French et al. (2015), a time series of hook echo mean Z_{DR} (dB) for three ranges of binned Z_H values during the life cycle of the tornado on 5 Jun 2009. The red dotted line represents the maximum difference in radial velocity recorded for the tornado after genesis and up to dissipation. (b) From Trapp et al. (2017), a scatterplot showing the relationship between midlevel updraft area (km^2) and near-ground vertical vorticity (s^{-1}). The values of updraft mesocyclone area represent peaks over an evaluation period between the time of storm split and the time of maximum near-ground vertical vorticity. (c) From Dawson et al. (2015), the magnitude of hydrometeor size sorting (HSS_{mag}) vs storm-relative helicity for the hodographs and random storm motions shown in their Fig. 6. (d) From Loeffler et al. (2020), composite time series of separation angle deviation from orthogonal orientation for tornadic cases (red line) and nontornadic cases (blue line). Light red and gray vertical bars for tornadic cases and light blue and yellow verticals bars for nontornadic cases represent bootstrapped confidence intervals at the 95% and 75% level. Red stars indicate a time interval where the difference in composite separation orientations is statistically significant at the 99% level using a two-sample *t* test.

K_{DP} highlights regions of a storm where a radar pulse encounters more liquid water in the horizontal dimension than in the vertical. Unlike Z_{DR}, K_{DP} is sensitive to number concentration, so a localized enhancement in K_{DP} is indicative of heavy precipitation comprising a large quantity of drops. Therefore, the observed changes in hook echo Z_{DR} and K_{DP} may be indicative of a change in the strength of the RFD via changes in evaporation rate. The Z_{DR} and K_{DP} dissipation relationships have not been analyzed in a large sample of tornado dissipation cases.

b. Z_{DR} column physical characteristics

One defining feature of a supercell is its rotating updraft: the mesocyclone. A ubiquitous feature of supercell thunderstorms, it is reasonable to hypothesize that the mesocyclone's evolution and/or physical characteristics could provide information regarding a storm's propensity for the formation of a tornado. Trapp et al. (2017) recently hypothesized, based on angular momentum and circulation arguments and simulations presented in their study, that a strong relationship exists between the scale of these features and the scale of the updraft (Fig. 1b). Such a relationship may also be driven by vertical wind shear, which has been shown to strongly modulate updraft width (e.g., Kirkpatrick et al. 2009), likely via faster storm motions that increase storm-relative low-level flow (Warren et al. 2017) and increase boundary layer mass flux (Peters et al. 2019). Thus, quantifying the updraft area, and monitoring decreases in area during an ongoing tornado, could provide useful insight into tornado dissipation if such a decrease is indicative of decreasing angular momentum and/or slower low-level storm-relative winds in the near-storm environment.

One possibility for quantifying updraft area is to objectively identify polarimetric radar signature supercell updraft proxies. Supercell updrafts are intense (>20 m s^{-1}) and act to loft liquid

water particles and small hail above the freezing layer, creating a localized area of enhanced Z_{DR} collocated with the storm's updraft/mesocyclone. Recent efforts to automate the detection of this signature (known as the Z_{DR} column; Illingworth et al. 1987; Kumjian et al. 2014) by Snyder et al. (2015) and Kingfield and Picca (2018) have provided tools that may be used for quantifying physical characteristics of this updraft proxy (e.g., Kuster et al. 2019). In addition, Van Den Broeke (2017), using a 0.5-dB threshold for the Z_{DR} column, noted *increases* in column area between genesis and dissipation in several cases. Despite these mixed results, a second relationship to investigate is that between a decreasing Z_{DR} column area and tornado dissipation.

c. Z_{DR} arc

One polarimetric feature that is present in most supercells is a localized enhancement of Z_{DR} located along the inflow edge of the forward flank region owing to hydrometeor size sorting (HSS). This enhancement, known as the "Z_{DR} arc," was hypothesized by Kumjian and Ryzhkov (2009) to result from strong vertical wind shear and to be related to the storm-relative helicity (SRH). Using a crude model, the authors found that a strong positive linear relationship exists between the magnitude of the Z_{DR} arc and 0.4–3-km SRH, which has shown some ability to discriminate between tornadic and nontornadic supercells (Thompson et al. 2012). Dawson et al. (2014) formalized the relationship as being driven by the deep-layer SR mean wind, and Dawson et al. (2015) found a positive correlation between the magnitude of HSS and the magnitude of the SRH in two supercell cases (Fig. 1c). As SRH and the SR mean wind both typically increase for increasingly off-hodograph motions, a common occurrence in most supercells (Bunkers et al. 2000), the magnitude of the Z_{DR} arc can be used as a proxy for SRH in supercells. Previously, Van Den Broeke (2017) noted no significant changes in the mean Z_{DR} value within the arc from genesis to demise in their averaged sample, though peak value was not interrogated. Consequently, the third relationship to be investigated is whether the peak magnitude of the Z_{DR} arc decreases, indicating a decrease in the SRH, leading up to tornado dissipation in supercells.

d. Low-level hail areal extent

Another polarimetric signature that is present in most supercells is indicative of inferred large hail. The Z_H and Z_{DR} can be used to detect large hail near the surface (e.g., Heinselman and Ryzhkov 2006) and, although the hail signature results from different processes ongoing within the storm than tornadoes, previous studies have shown differences in the hail signature's physical characteristics between tornadic and nontornadic supercells. In a small sample of supercell storms, Kumjian and Ryzhkov (2008a) found the large-hail signature to be more persistent throughout the storm life cycle in nontornadic storms than in tornadic storms. Somewhat consistent with this finding, Van Den Broeke (2016) showed that the hail signature's areal extent was smaller in tornadic supercells compared to nontornadic supercells, and Van Den Broeke (2017) found increases in hail areal extent between tornadic and nontornadic times within the same storm, though the area was normalized to storm size and the increases were not significant.[1] Furthermore, Van Den Broeke (2020) investigated several supercells and found that the hail signature's areal extent tended to be smaller in "pretornadic" supercells than in nontornadic supercells. The author did not hypothesize why there may be a relationship between hail area and tornado formation and did not investigate the relationship between hail signature areal extent and the life cycle of a tornado. However, Dennis and Kumjian (2017) found that increases in low-level vertical wind shear and low-level SRH led to smaller hail in their simulated supercells. Using the same storm environments, Kumjian and Lombardo (2020) found that such greater low-level shear led to faster embryo advection across the hail growth region, resulting in less residence time and thus smaller hail. Smaller, melting hail could lead to an increase in the observed Z_{DR}, which could diminish the area of the large-hail signature. Thus, a fourth signature to investigate is whether the large hail areal extent increases, potentially an indication of decreased low-level vertical wind shear and SRH, leading up to tornado dissipation.

e. Z_{DR}–K_{DP} separation vector

During HSS, large drops are carried through the storm by the deep-layer SR mean wind and deposited along the inflow edge of the forward flank region, resulting in the Z_{DR} arc. In turn, smaller drops are advected farther into the storm as their slower fall speeds allow for them to remain in the sorting layer for a longer duration. The area in which these relatively smaller drops are deposited is known as the "K_{DP} foot" (Romine et al. 2008) and is characterized by lower Z_{DR} owing to their smaller median drop size, but high K_{DP} given the large number concentration of drops. Loeffler and Kumjian (2018) investigated the relationship between the "separation vector" of these two enhancement regions and tornadogenesis in 30 nonsupercellular tornadic storms. Separation distance (i.e., the length of the vector) was found to peak around the time of the tornado report, whereas the separation orientation, calculated as degrees clockwise from the storm motion vector, tended to become more orthogonal relative to storm motion around the same time. Loeffler et al. (2020) extended this technique to tornadic and nontornadic supercells and found that there was a statistically significant difference in separation orientations between the two storm types (Fig. 1d). *Specifically, separation orientations were more orthogonal relative to storm motion in tornadic supercells, whereas nontornadic supercells had more parallel orientations.* Their study focused on a 40-min interval centered on the presumed time of tornadogenesis/tornado failure, but there is a trend in their data toward a more parallel orientation of the separation vector later in the tornado life cycles (Fig. 1d). Follow-up modeling work in Loeffler and Kumjian (2020) found that separation vector orientation is related both to the storm-relative winds and the storm-relative helicity magnitude in the sorting layer. Therefore, a fifth signature to investigate is whether separation vectors transition to

[1] The author found the increase to be "weakly significant" based on a p value of 0.083.

TABLE 1. A list of the 36 tornadic supercell cases used for this study, including the date of the event, the maximum damage rating achieved, and the times analyzed (in UTC) for this study.

Date	Closet WSR-88D	Damage rating	Times analyzed (UTC)
15 Apr 2012	KVNX	EF0	0106–0124
14 Apr 2012	KICT	EF3	0218–0238
18 Mar 2013	KFFC	EF2	2213–2232
19 May 2013	KTLX	EF3	2332–2349
20 May 2013	KTLX	EF4	2018–2035
10 Jun 2013	KHPX	EF2	1846–1904
17 Nov 2013	KPAH	EF2	2034–2052
28 Apr 2014	KLZK	EF3	0045–0103
28 Apr 2014	KGWX	EF2	2258–2313
29 Apr 2014	KHTX	EF3	0114–0129
10 May 2014	KEAX	EF2	2215–2234
22 May 2014	KENX	EF3	1948–2008
27 Jun 2014	KLCH	EF0	1840–1859
7 Jul 2014	KMQT	EF0	0113–0137
6 May 2015	KICT	EF3	2155–2215
6 May 2015	KUEX	EF2	2159–2221
6 May 2015	KTLX	EF3	2202–2224
9 May 2015	KDYX	EF3	2143–2203
16 May 2015	KFDR	EF2	2330–2345
6 Jun 2015	KGLD	EF0	0253–0309
20 Jun 2015	KUDX	EF2	0304–0328
16 Nov 2015	KDDC	EF3	0055–0117
17 Nov 2015	KDDC	EF2	0027–0055
31 Mar 2016	KINX	EF1	0028–0057
10 May 2016	KPAH	EF3	1957–2018
24 May 2016	KDDC	EF3	2256–2323
24 May 2016	KDDC	EF2	2351–0010
17 Sep 2016	KMAF	EF1	0017–0036
7 Feb 2017	KLIX	EF2	1641–1700
1 Mar 2017	KVWX	EF3	0429–0447
12 Jun 2017	KCYS	EF2	2244–2302
11 Jul 2017	KMVX	EF2	0027–0049
31 Aug 2017	KGWX	EF2	2102–2128
8 Oct 2017	KGSP	EF2	2102–2128
20 May 2018	KGRK	EF1	1324–1343
1 Dec 2018	KILX	EF1	2314–2338

more parallel orientations prior to tornado dissipation owing to decreases in SRH.

3. Data and methods

In this study, we use WSR-88D Level-II traditional moment and polarimetric data in 36 tornadic supercells. Analysis for each case began with quality-controlled data (see section 3a) of the whole storm; data were then analyzed from specific regions of the storm depending on what polarimetric radar signature was being evaluated. The specific radar variables analyzed include the radar reflectivity factor (Z_H; dBZ), Z_{DR} (dB), K_{DP} (° km^{-1}), and copolar cross correlation coefficient at lag zero (ρ_{hv}). Derived radar products include median drop size (D_0; mm) and total number concentration (N_T; m^{-3}) (Cao et al. 2008).

The 36 tornadic supercell cases analyzed in this study were selected identically to those in FK19, though the number analyzed for each behavior varies. All recorded supercellular tornadoes in the Storm Prediction Center (SPC) Convective Mode database were considered. Only cases that we categorized as "long-duration" tornadoes—cases with at least four consecutive volumes of WSR-88D data available while the tornado is ongoing leading up to and including dissipation (for a minimum of four scans, five being preferred)—were analyzed, so that each case had ~15–20 min of data available for study. A full volume update was required, and any supplemental SAILS scans were omitted to maintain consistency between radars. Additionally, storms undergoing cyclic tornadogenesis were not included to isolate trends prior to dissipation. Furthermore, only tornadoes observed within 60 km of the radar site and outside of the "cone of silence" in all scans were analyzed. The range requirement ensures that, given the appropriate elevation angle, every storm was sampled at a center-beam height of ~500 ± 150 m, a height level at least broadly representative of near-surface evolution. For this study, 28 of the 36 storms from 2012 to 2016 used in FK19 were deemed acceptable. An additional eight storms from 2017 to 2018 were added to the FK19 dataset, giving this study the same 36-case sample size as FK19 (Table 1). The cases

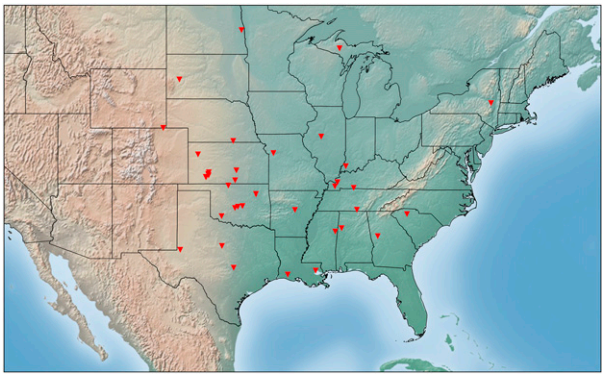

FIG. 2. Map of "long-duration" tornado cases ($n = 36$) used in this study.

analyzed in this study are broadly representative of supercells in general; storms selected ranged across the spectrum of supercell morphologies, occurred in 18 states over multiple regions of the continental United States (Fig. 2), and formed in both warm and cold seasons. However, we cannot rule out that weaker and/or shorter-duration tornadoes may respond differently to the hypothesized mechanisms and conditions supportive of tornado dissipation. Once selected, cases were manually examined to ensure that the radar data are of high quality (i.e., no noise contamination), storm interactions are minimized, and no radar artifacts contaminate the data.

a. Z_{DR} bias correction and differential attenuation

Analysis of the five signatures rely most heavily on accurate Z_{DR} data, which is subject to large biases and differential attenuation. For biases, we ensure accurate Z_{DR} analysis by replicating the exhaustive Z_{DR} calibration methodologies of the NWS's Radar Operations Center (ROC; e.g., Richardson et al. 2017) as described in Tuftedal et al. (2021). Regarding differential attenuation, hook echoes and Z_{DR} columns occur in areas where signal loss is rare. Any case exhibiting significant signal loss in the area of the Z_{DR} arc, large hail signature, and K_{DP} maximum was not analyzed.

b. Polarimetric radar signatures

1) HOOK ECHO RAINDROP SIZE

Identification of the hook echo region is done subjectively following the methodology of French et al. (2015) and Tuftedal et al. (2021). For the elevation angle scan closest to a height of 500 m, the hook echo was enclosed within a manually created polygon. Flanking lines and new cells generated by outflow in the RFD region were omitted from the hook polygon, and the TVS was required to be located within the polygon to ensure we were sampling the environment near the tornado. The TVS was defined the same way as in FK19 (i.e., $\Delta V > 15$ m s^{-1} separated by a distance < 1.5 km). In an effort to limit subjectivity, both the first and second author separately examined and modified all polygons so as to best match the polygon with the aforementioned visual guidelines (polygon files are available upon request). Hook echo median raindrop size and number concentration were estimated using the relationships established in Cao et al. (2008) and used in Tuftedal et al. (2021).

2) Z_{DR} COLUMN PHYSICAL CHARACTERISTICS

To identify the Z_{DR} column, a novel algorithm was developed for use within the Warning Decision Support System-Integrated Information (WDSS-II; Lakshmanan et al. 2007). Radar data were filtered using a ρ_{hv} threshold of 0.8 to mitigate contamination from nonmeteorological scatterers. Once filtered, the Z_{DR} column was identified by locating the region column was identified by locating the region ~1 km above the environmental 0°C level of $Z_{DR} > 1.0$ dB collocated with the storm's hook echo/updraft (Fig. 3). Radar gates that fit the given criteria had their areas calculated; neighboring gates which also met the criteria were considered one region and their areas were summed. The largest contiguous region area was recorded for each volume (we also examined a summed region, but areas and temporal trends in areas were similar for both sets). Environmental 0°C levels were identified using the RAP model output analyzed at the nearest grid point to the median latitude/longitude of the hook echo polygon defined in section 3b(1). Model run times closest to that of the time of the radar volume were used to ensure the environment is being captured as representatively as possible.

This approach, while providing a good estimate of the Z_{DR} column, is not without its shortcomings. First, while steps were taken to mitigate the effects of Z_{DR} bias, it is likely that some affected gates were still included, and the calculated area was artificially inflated. Second, the bin size for each column calculated is dependent on the range from the radar meaning that fewer gates at a longer range would have the same area as more bins closer to the radar. Third, any attenuation/interaction from precipitation between our storm of interest and the radar could cause lower power returns and alter the Z_{DR}, and therefore the calculation of the column area. While prudent to acknowledge this potential shortcoming, we did not have any issues with obvious attenuation. Finally, higher elevation angles have steeper angles of ascent so that the same vertical displacement would occur over a smaller horizontal area. This means that column areas calculated using higher elevation angles could potentially include gates from the melting layer, which would artificially inflate the size of the column. However, given that this is a ubiquitous problem for radar, the results from this method are close to what forecasters would see in real time.

3) Z_{DR} ARC

Using WDSS-II, Z_{DR} arc parameters were identified manually in the forward flank region of the supercell, along the Z_H gradient where the arc is found. To identify the Z_{DR} arc, radar gates with $\rho_{hv} < 0.93$ were eliminated (Loeffler and Kumjian 2018); as small melting hail contributes to the Z_{DR} arc signature, a slightly lower ρ_{hv} filter was used in lieu of the aforementioned 0.97 threshold. Once filtered, we used a dynamic Z_{DR} threshold (Fig. 4), similar to that used in Loeffler and Kumjian (2018), to define the arc in a relative sense rather

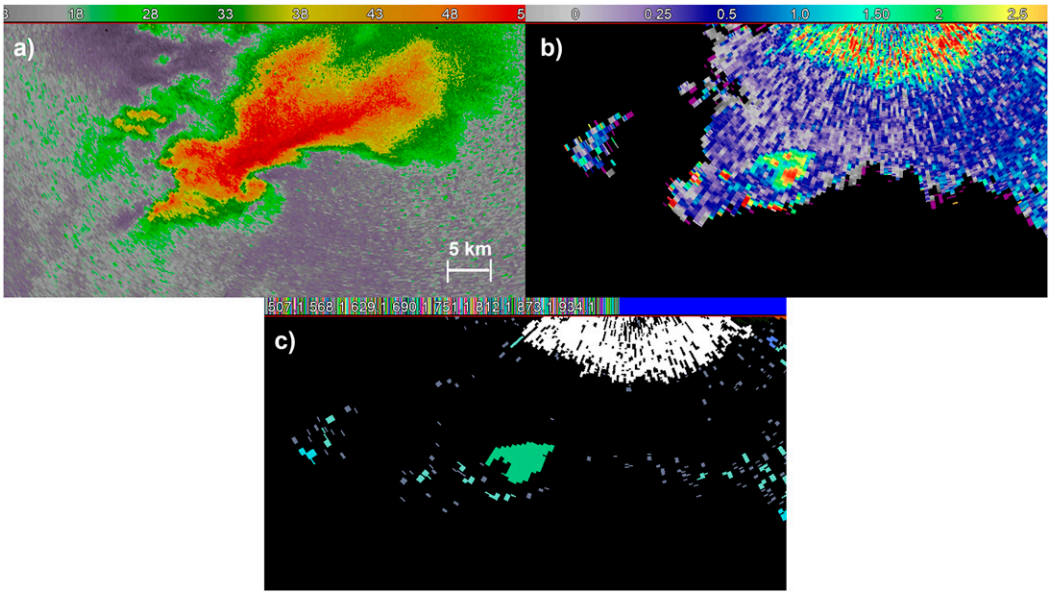

FIG. 3. Example of the identification of the Z_{DR} column's areal extent for the 15 Apr 2012 case observed by KICT. PPIs displayed in WDSS-II of (a) Z_H, (b) Z_{DR}, and (c) output from the Z_{DR} column area identification algorithm are shown. The contiguous area of the Z_{DR} column shown in (c) is 51.07 km^2.

than a "one-threshold-fits-all-cases" approach. Data at the elevation angle closest to a height of 500 m were thresholded every 0.5 dB, starting at 2.0 dB, and the highest threshold value that allowed for $n \geq 10$ radar gates was used as the "dynamic" threshold for arc definition. A dynamic threshold is appropriate because Z_{DR} arcs, although ubiquitous in supercells, take on a variety of appearances and their evolution may be sensitive to what threshold value is used to identify the feature. Once the arc was identified for each case, its maximum magnitude was estimated by using the highest Z_{DR} value to occur within at least two of its gates. The use of the highest magnitude to occur within at least two gates, in addition to the range requirement, mitigate issues caused by differing gate resolution.

4) LOW-LEVEL HAIL AREAL EXTENT

A new algorithm was developed for use in WDSS-II. Radar data closest to the 500-m altitude with $\rho_{hv} > 0.8$, $Z_H \geq 55$ dBZ, and -0.5 dB $\leq Z_{DR} \leq 1.0$ dB (Ryzhkov et al. 2013) were retained. The ρ_{hv} threshold of 0.8 allows for the presence of hail within the volume, but mitigates any contamination by debris or

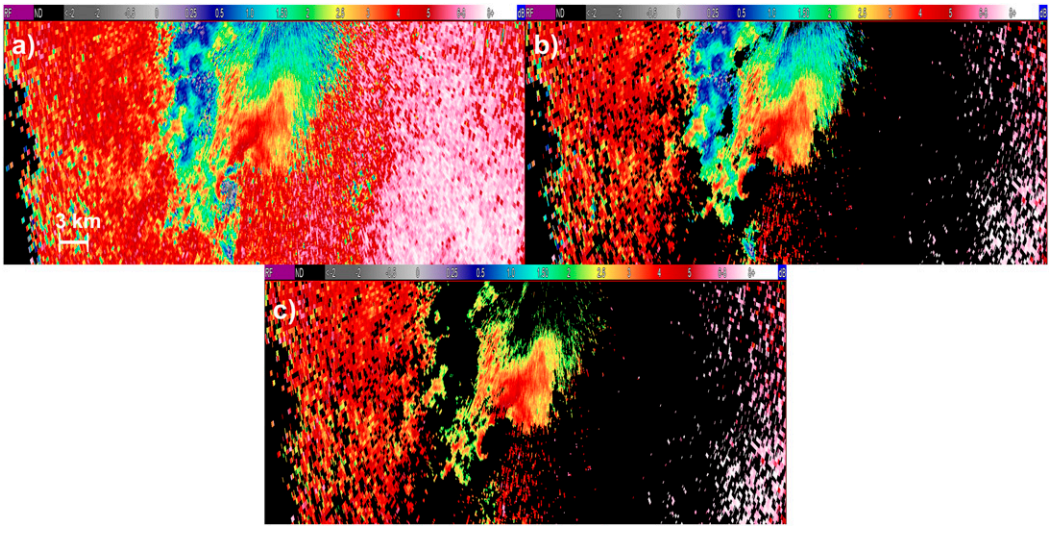

FIG. 4. Example of the adaptive threshold applied to identify the Z_{DR} arc for the 15 Apr 2012 case observed by KICT. Data shown are PPIs of Z_{DR} from WDSS-II with (a) no threshold applied, (b) a ρ_{HV} filter of 0.93 applied, and (c) a ρ_{HV} filter of 0.93 and a 2-dB Z_{DR} filter applied. The maximum magnitude of the Z_{DR} arc shown in (c) is 5.51 dB.

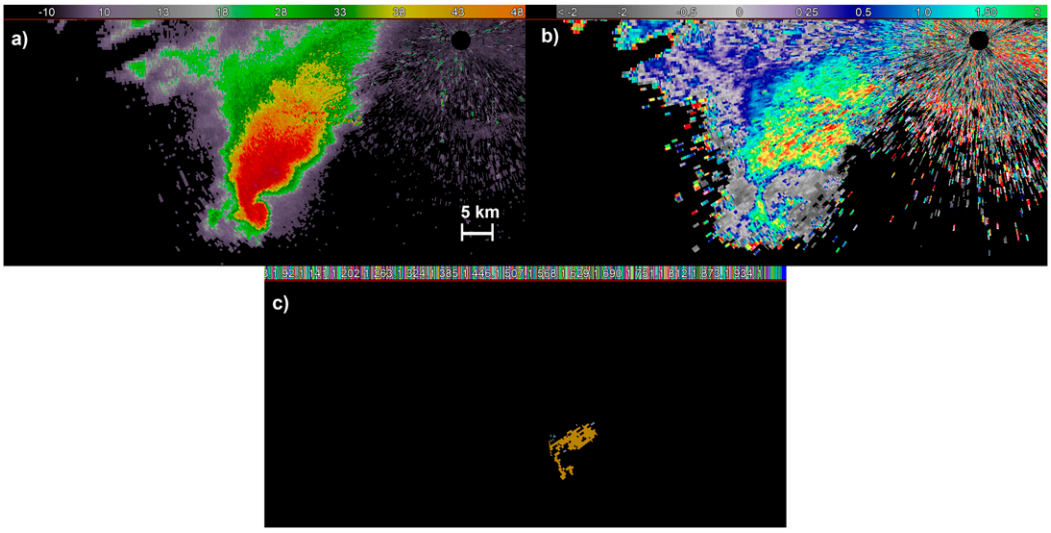

FIG. 5. Example of the identification of the large hail signature's areal extent for the 17 Nov 2015 case observed by KDDC. PPIs displayed in WDSS-II of (a) Z_H, (b) Z_{DR}, and (c) output from the large hail signature identification algorithm are shown. The total large hail areal extent shown in (c) is 38.58 km^2.

biological scatterers. Once filtered, the large hail signature area (Fig. 5) was calculated in a manner identical to the Z_{DR} column. The largest contiguous area, as well as the total storm summed area, was recorded for each volume leading up to dissipation.

5) Z_{DR}–K_{DP} SEPARATION VECTOR

To identify the Z_{DR} and K_{DP} enhancement regions, we again applied the same "dynamic threshold" approach of Loeffler and Kumjian (2018) to both the Z_{DR} and K_{DP} fields. After a ρ_{hv} threshold of 0.93 was applied to ensure meteorological returns, gates which met the dynamic threshold requirements were considered the Z_{DR} and K_{DP} enhancement regions. Here, $n \geq 25$ gates were required to determine the dynamic threshold, to be consistent with Loeffler et al. (2020). Radar gates were mapped to a Cartesian coordinate system centered on the radar; centroids were calculated from the median x and y coordinates from every gate in each region and the distance and orientation relative to storm motion (the two components of the "separation vector") were calculated from the two centroids. Separation vector components were then analyzed throughout the period of interest for each storm.

c. *Statistical significance testing*

Statistical testing was completed using the Wilcoxon signed-rank test, a nonparametric test that establishes whether paired data (in this study, one of the four storm-scale polarimetric features from two different volumes in the same storm) have mean ranks that differ significantly from zero (Wilcoxon 1945). The use of this test limits the influence of outliers and eliminates the often-equivocal assumption that the underlying population is normally distributed. The version used in this study is directional (e.g., it is hypothesized that Z_{DR} should be larger in the dissipation volume than in previous volumes), applies a continuity correction,[2] and follows the method proposed by Pratt (1959) of including zero differences in the ranking process. In the interest of leveraging the information found in this study for future nowcasting applications, and in support of changing best practices for statistical testing, only "very significant" differences, those with a statistical significance level of 1% ($p \leq 0.01$), are highlighted. Also, as in FK19, combinations of storm-scale and TVS behaviors that portend tornado dissipation were examined.

4. Observations of dual-pol signatures associated with dissipation

After examination of each case to ensure sufficient data quality, it was determined that 36 cases could be analyzed for the hook echo portion of this study, 32 cases for the Z_{DR} arc portion, 25 cases for the Z_{DR} column portion, 31 cases for the large hail signature portion, and 32 cases for the Z_{DR}–K_{DP} separation vector portion. Ideally, for each case, the four scans prior to tornado dissipation in addition to the dissipation volume were examined, but cases with usable data for only three scans prior to dissipation plus the dissipation volume also were permitted for analysis. Radar volumes are labeled based on the number of scans prior to "D," which represents the last volume in which the TVS was observed. The radar variables analyzed were grouped into their corresponding volumes relative to dissipation (i.e., "$D - 4$" is four scans prior to D). As this study is focused on trends leading up to dissipation to assess the possibility of nowcasting tornado decay, we did not investigate volumes that occurred after the

[2] The continuity correction adjusts the Wilcoxon rank statistic by 0.5 toward the mean value when computing the z statistic. This is necessary for Python's Scipy module for sample sizes larger than 25.

tornado had dissipated (i.e., volume "$D + 1$"). Each signature was identified and interrogated as described in section 3b, and simultaneous occurrences of storm-scale and TVS behaviors also were investigated.

There are six hypotheses that will be partially tested in this study:

- an increase in hook echo median raindrop size and/or concentration portends tornado dissipation owing to an increase in evaporation rates and an intrusion of more negatively buoyant air;
- a decrease in Z_{DR} column area precedes tornado dissipation as a proxy signature of updraft weakening and/or decreases in vertical wind shear;
- a decrease in the magnitude of the Z_{DR} arc is observable leading up to tornado dissipation owing to weaker SRH being ingested by the storm's low-level updraft and/or tornado;
- an increase in the hail signature's areal extent portends tornado dissipation owing to a weakening of low-level vertical wind shear being ingested by the storm's low-level updraft and/or tornado;
- a trend toward a more parallel orientation in Z_{DR}–K_{DP} separation vector orientation angle precedes tornado dissipation owing to a reduction in the magnitude of SRH being ingested by the storm's low-level updraft and/or tornado;
- simultaneous occurrence of multiple identified dissipation behaviors is strongly preferred at or near dissipation time compared to 15–20 min prior to dissipation.

a. *Hook echo raindrop size*

Hook echo median Z_{DR} tends to increase subtly leading up to tornado dissipation by a median value of ~0.1 dB, between volumes $D - 4$ and D (Fig. 6a). However, between volumes $D - 3$ and D, it stays nearly constant (i.e., a change of only −0.02 dB). Between $D - 4$ and D, Z_{DR} increases in 19/29 cases (Fig. 6b). Five cases exhibit a large (>0.5 dB) increase in Z_{DR}, whereas two cases exhibit a large (>0.5 dB) decrease in Z_{DR}. Similar results are found between volumes $D - 3$ and D. The two storms with large Z_{DR} decreases are observed to interact with another cell before dissipation, but cell interactions are not unique to storms with Z_{DR} reductions. Median volume-to-volume changes (i.e., changes from $D - 4$ to $D - 3$, from $D - 3$ to $D - 2$, etc.) are positive for all intervals (Fig. 6c), but no interval is statistically different from the final volume-to-volume (i.e., from $D - 1$ to D) change. Similarly, the results for

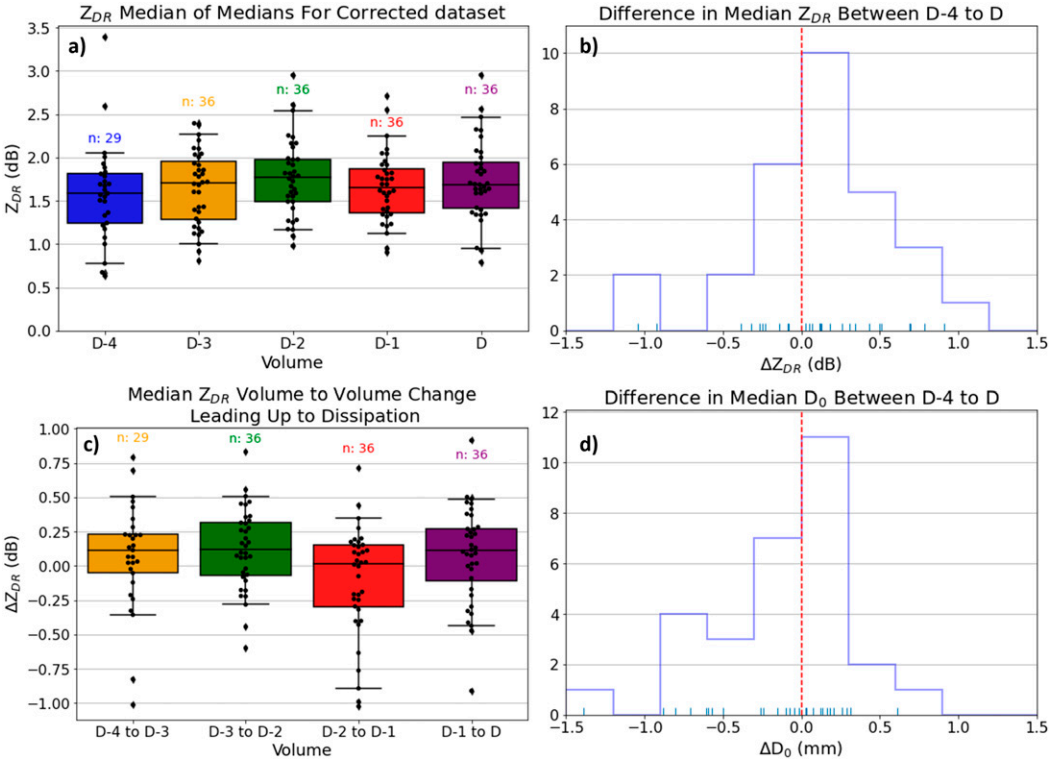

FIG. 6. Boxplots showing the (a) distribution of hook echo median Z_{DR} values (dB), for n cases, for 4, 3, 2, and 1 scans prior to dissipation, as well as the last scan in which the tornado was identified in radar data (D); (b) histogram showing the distribution of hook echo median Z_{DR} differences (dB) between the fourth scan prior to dissipation ($D - 4$) and the final scan before the tornado dissipated (D); (c) the volume-to-volume differences in hook echo median Z_{DR}; and (d) as in (b), but for D_0. The whiskers in (a) and (c) represent the 5th and 95th percentiles. If the volume label in (c) appears in red, then the null hypothesis that the difference between the population mean ranks of those two volumes are zero can be rejected at the 1% level (p value ≤ 0.01) using a direction Wilcoxon signed-rank test. The dashed red lines in (c) and (d) denote the 0.0-dB difference line, and the short blue lines represent the values of the data.

estimated D_0 (Fig. 6d) show no real trend. That both Z_{DR} and D_0 show no signal contradicts our hypothesis that hook echo median raindrop size increases leading up to tornado dissipation.

The same methods for analysis were applied to K_{DP} and N_T. From $D - 4$ to D, the median increase in K_{DP} is 0.21° km^{-1} and the distribution at $D - 3$ is different from that at D at the 99% level (Fig. 7a). From $D - 4$ to D, K_{DP} increases in 19/29 cases (Fig. 7b), with eight cases experiencing large (>0.5° km^{-1}) increases and two with large (>0.5° km^{-1}) decreases; similarly, K_{DP} is observed to increase in 26/36 cases from $D - 3$ to D (not shown). The median increase in K_{DP} during this time interval is 0.18° km^{-1}. Median volume-to-volume changes in K_{DP} (Fig. 7c) are positive for all intervals, but no interval is significantly different from the final interval at the 99% level.

The N_T results are similar to K_{DP}: median N_T increases by 0.29 m^{-3} from $D - 4$ to D and the distributions at volumes $D - 4$ and $D - 3$ are significantly different from that at volume D at the 99% level (Fig. 8a). From $D - 4$ to D, 21/29 cases (Fig. 8b) exhibit an increase in median N_T, and 11 cases increase by a "large" amount of 0.5 m^{-3} or more. One case decreases by more than 0.5 m^{-3}. Similar to K_{DP}, median N_T increases from volume-to-volume (Fig. 8c), but no interval is significantly different from the final interval at the 99% level. The visual K_{DP} progression (Fig. 9) is shown for an example case which displays "large" increases in both K_{DP} and N_T prior to tornado dissipation. The Z_H (Figs. 9a,d,g,j) and radial velocity (Figs. 9b,e,h,k) show little obvious indication of a dissipating tornado leading up to volume D, whereas there is a clear migration of enhanced K_{DP} values (Figs. 9c,f,i,l) from the forward flank region into the hook echo region. The K_{DP} and N_T results, while not originally included in our hypothesis, do still support the idea that potentially less buoyant air is being introduced into the storm's updraft.

b. Z_{DR} column physical characteristics

The Z_{DR} column contiguous area decreases from $D - 4$ to D with a median decrease of 4.07 km^2 (Fig. 10a). From $D - 4$ to D, 13/21 cases display a decrease in Z_{DR} column area (Fig. 10b), and no volume is found to be significantly different from the distribution at D. Volume-to-volume changes in contiguous area were calculated and boxplots were constructed (Fig. 10c). Whereas the median change in Z_{DR} column contiguous area is positive from $D - 4$ to $D - 3$, the median change is negative from volume-to-volume for the three remaining time periods. The largest single median decrease in Z_{DR} column contiguous area occurs between $D - 2$ and $D - 1$, but the largest increases also occur between these two volumes. The observed trend for Z_{DR} column contiguous area to decrease ostensibly supports our hypothesis that updrafts shrink leading up to dissipation. However, the relationship is not statistically robust, with several cases demonstrating updraft expansion leading up to dissipation, and perhaps indicates a more complex relationship than the one hypothesized.

c. Z_{DR} arc

The Z_{DR} arc maximum magnitude is observed to decrease from $D - 4$ to D, with a relatively large median decrease of 0.43 dB (Fig. 11a). The distribution at $D - 3$ is found to be significantly different from that at volume D at the 99% level. From $D - 4$ to D, Z_{DR} arc maximum magnitude decreases in 17/24 cases (Fig. 11b). The median Z_{DR} arc maximum

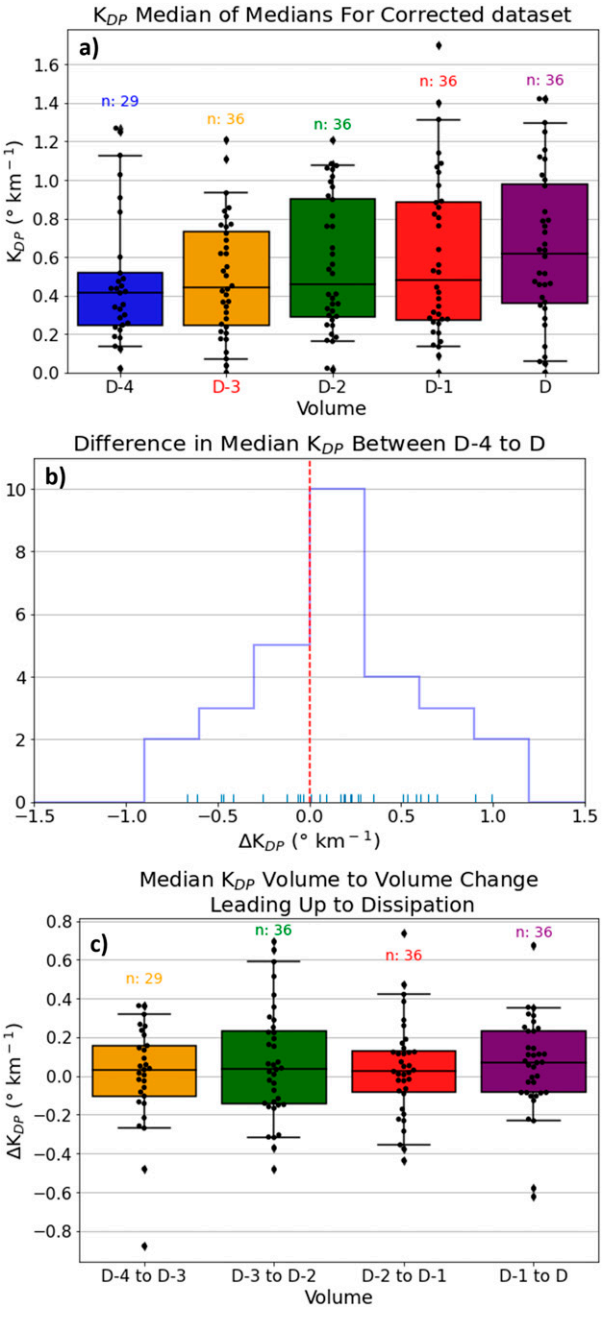

FIG. 7. (a) As in Fig. 6a, but for hook echo median K_{DP} (° km^{-1}); (b) as in Fig. 6b, but for hook echo median K_{DP}; and (c) as in Fig. 6c, but for hook echo median K_{DP}. If the volume label for $D - 1$, $D - 2$, $D - 3$, or $D - 4$ in (a) appears in red, then the null hypothesis that the difference between the population mean ranks of that volume and volume D is zero can be rejected at the 1% level (p value ≤ 0.01) using a directional Wilcoxon signed-rank test.

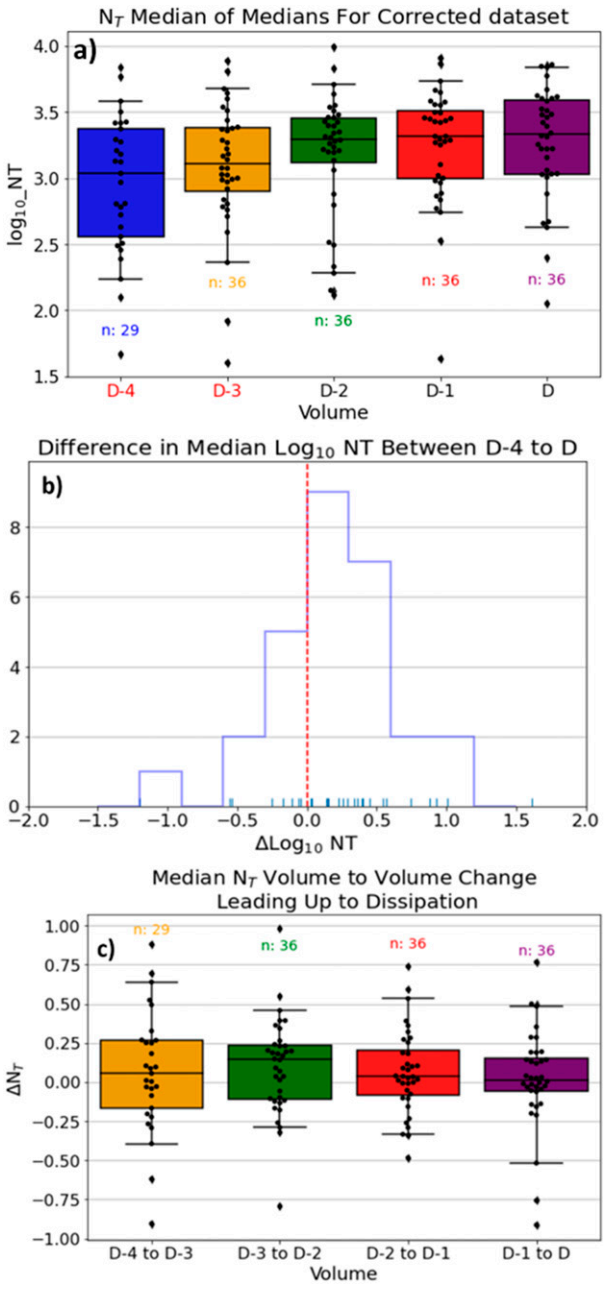

FIG. 8. (a) As in Fig. 6a, but for hook echo median N_T (m^{-3}); (b) as in Fig. 6b, but for hook echo median N_T; and (c) as in Fig. 6c, but for hook echo median N_T.

magnitude tends to increase from $D-4$ to $D-3$, but decrease thereafter until dissipation (Fig. 11c). The largest volume-to-volume change is between $D-3$ and $D-2$ with a median decrease of -0.21 dB. The visual progression of Z_H (Figs. 12a,d,g,j), radial velocity (Figs. 12b,e,h,k), and Z_{DR} (Figs. 12c,f,i,l) are shown for a case which saw a decrease in Z_{DR} arc maximum magnitude. Similar to the hook echo median K_{DP} case, Z_H and radial velocity do not show obvious signs of dissipation. However, the magnitude of the Z_{DR} arc clearly diminishes leading up to dissipation. The observed trend in Z_{DR} arc maximum magnitude supports our hypothesized relationship.

d. *Large hail signature areal extent*

For the large hail signature, both the largest contiguous area and the total large hail area were recorded for each volume. From $D-4$ to D, the median changes in contiguous and total hail area are 0.04 km^2 and -0.07 km^2, respectively (Figs. 13a,c). For reference, the approximate area of a radar gate at a range of ~30 km is ~0.119 km^2. Volume-to-volume plots were constructed (Fig. 13b), but no obvious signal is apparent. From $D-4$ to D, there is an increase in total areal extent in 12/24 cases (Fig. 13d). Most times exhibit large variability and numerous outliers, but there is no evidence to the support the hypothesized relationship.

e. *Z_{DR}–K_{DP} separation vector*

From $D-4$ to D, the median separation orientation angle is observed to decrease by 6.9° (Fig. 14a). The distribution at $D-3$ is significantly different from that at D at the 99% level. Separation orientation angle decreases from $D-4$ to D in 17/26 cases (Fig. 14b). Median volume-to-volume changes in separation angle (Fig. 14c) show no clear trend; increases in median separation angle occur from $D-4$ to $D-3$ and from $D-2$ to $D-1$, whereas decreases are observed from $D-3$ to $D-2$ and from $D-1$ to D. The largest change is between $D-1$ and D with a median decrease of $-9.93°$, but no interval is significantly different from the final volume at the 99% level. That separation angles decrease supports our hypothesis that separation angles move toward a more parallel orientation leading up to dissipation. Separation distance decreases in 15/26 cases (not shown) with a median decrease of 0.30 km. Conversely, from $D-3$ to D, the separation distance increases in 20/32 cases with a median increase of 0.56 km. No volume is significantly different from the final volume for separation distance. Median volume-to-volume changes are negative for all but one interval (from $D-2$ to $D-1$), but no interval is significantly different from $D-1$ to D.

5. Summary and discussion

The primary conclusions from this study are that K_{DP} and N_T generally increase while Z_{DR} arc maximum magnitude and Z_{DR}–K_{DP} separation angle generally decrease in the time leading up to tornado dissipation. Although the K_{DP} and N_T results are different from our original hypothesis, this finding may still be indicative of a process that results in the same loss of positively buoyant air and/or addition of negatively buoyant air within the RFD region of tornadic supercells. That median hook echo Z_{DR} and D_0 show essentially no tendency to increase or decrease during this time, coupled with K_{DP} and N_T increasing, is indirect evidence that an influx of more raindrops (greater liquid water content) with relatively constant drop sizes into the RFD region may be detrimental to tornadic supercells. It is likely that mobile radars with high spatiotemporal resolution would be needed to identify (i) the region of the storm where the enhancement in liquid water content, if a real signal, originates and (ii) if there are

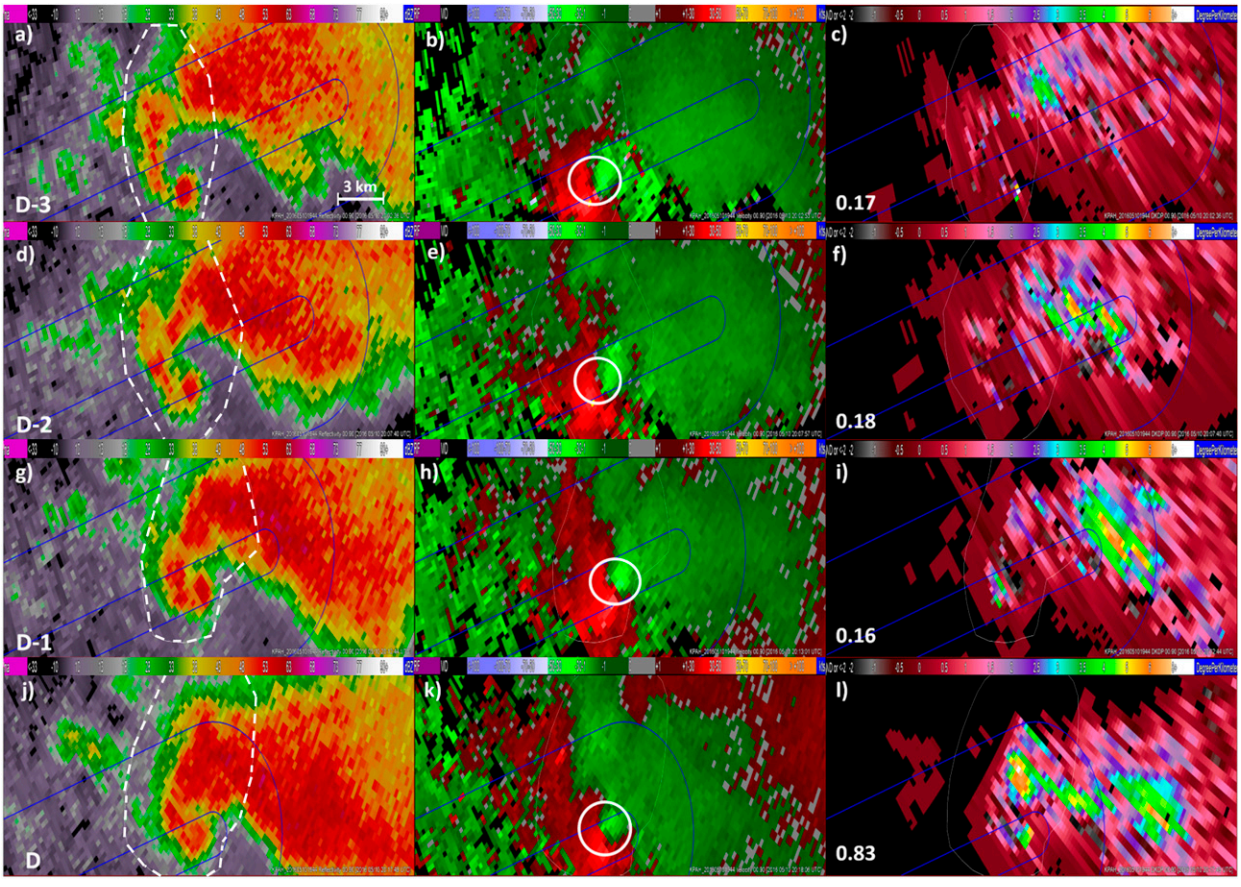

FIG. 9. PPIs displayed in WDSS-II showing the progression of (a),(d),(g),(j) Z_H; (b),(g),(h),(k) radial velocity; and (c),(f),(i),(l) K_{DP} for the 10 May 2016 case at four times: 2002:36, 2007:40, 2012:44, and 2017:49 UTC. Dashed white outlines approximately represent the subjectively identified hook for each scan, and thick white circles in (b), (e), (h), and (k) denote the TVS. The volume relative to dissipation is indicated in white text in (a), (d), (g), and (j), and the hook echo median K_{DP} (° km^{-1}) is shown in white text in (c), (f), (i), and (l). The blue oval marks the approximate tornado path.

subregions within the hook echo that are most relevant to impacting tornado dissipation, as suggested for tornadogenesis in Tuftedal et al. (2021). We also cannot comment on the thermodynamic environment nor clarify the role evaporation plays (e.g., may the *potential* for evaporation be important) without near-surface thermodynamic observations. Moreover, to ensure that observed signals (or a lack thereof) are indicative of processes related to dissipation, a larger dataset comprised of both dissipation and "maintenance" (i.e., the tornado weakened before strengthening again) cases would be beneficial. Regardless, we believe these results support further exploration of K_{DP} use in nowcasting tornado dissipation.

The Z_{DR} arc maximum magnitude decreases prior to dissipation are consistent with a weakening of the deep-layer SR wind and a decrease in near-storm SRH for storms with off-hodograph storm motions (i.e., supercells) owing to changes in storm motion. With less SRH for the storm to ingest, the storm may no longer be able to support an ongoing tornado with vorticity-rich air, contributing to its dissipation. However, one caveat exists in interpreting these results—as we allowed for melting hail to be included in the Z_{DR} arc, other processes (i.e., changes in updraft strength, precipitation type, etc.) can influence the magnitude of the arc. Despite this, and although there were cases that fluctuated between increasing and decreasing magnitude between radar volumes, monitoring the Z_{DR} arc maximum magnitude in the period 10–20 min before dissipation may have some utility for forecasters.

Overall, Z_{DR} column areas have a slight tendency to decrease in the volumes leading up to dissipation. Such a behavior would be consistent with our hypothesis, but the observed relationship is weak. One reason why this signature may not exhibit much of a signal: alterations in angular momentum near the updraft may be more important during tornadogenesis and less important once a tornado has formed. Z_{DR} column areas oscillate throughout the period in question for several storms and increases in column area leading up to dissipation are common. Thus, there is little evidence to support using Z_{DR} column area as a tool for nowcasting tornado dissipation.

There is no signal present for either method of quantifying the large hail signature leading up to tornado dissipation. Hail forms out of different storm processes ongoing within the updraft, and

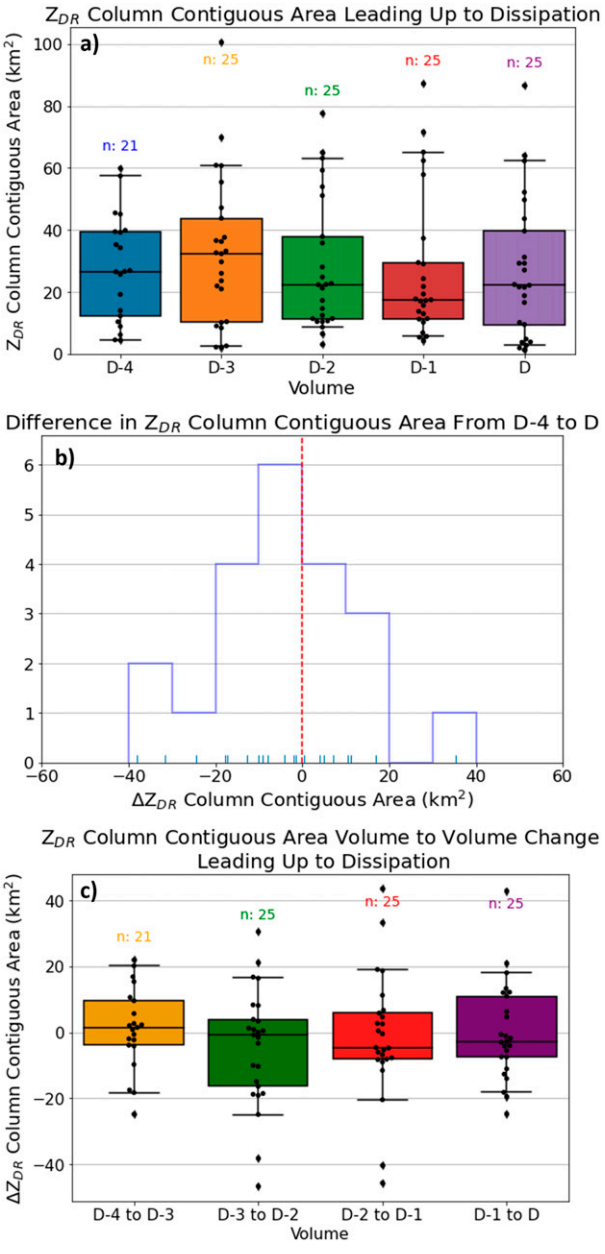

FIG. 10. (a) As in Fig. 6a, but for Z_{DR} column contiguous area (km^2); (b) as in Fig. 6b, but for Z_{DR} column contiguous area; and (c) as in Fig. 6c, but for Z_{DR} column contiguous area.

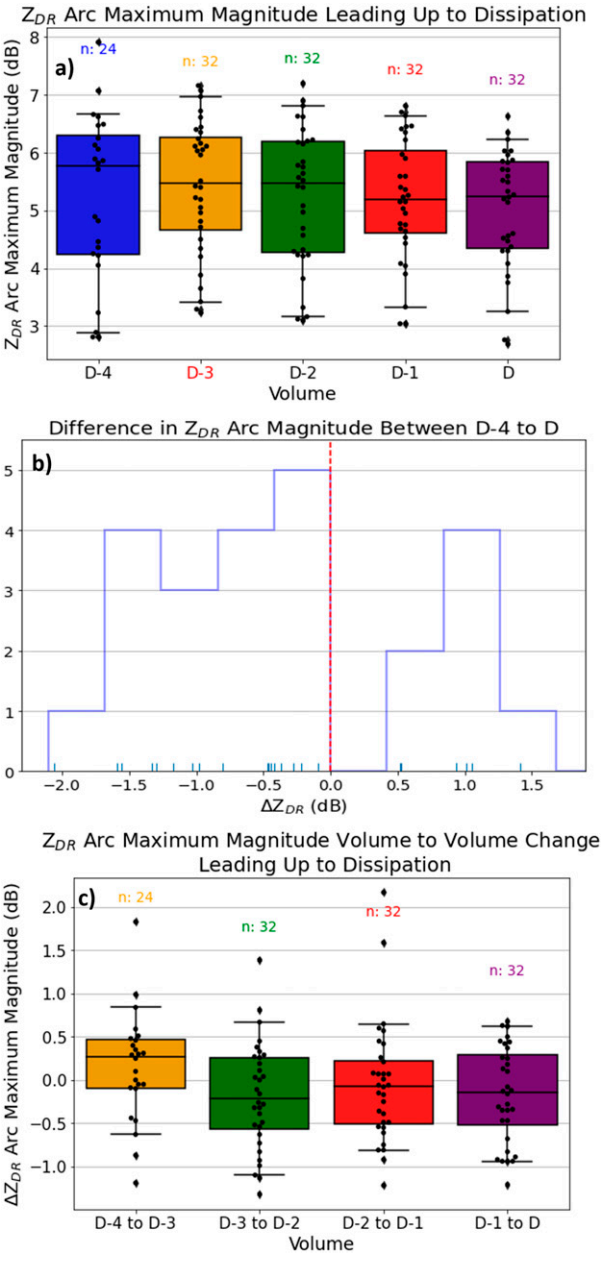

FIG. 11. (a) As in Fig. 6a, but for Z_{DR} arc maximum magnitude (dB); (b) as in Fig. 6b, but for Z_{DR} arc maximum magnitude; and (c) as in Fig. 6c, but for Z_{DR} arc maximum magnitude.

production is often controlled by various near storm environmental parameters (beyond just low-level shear) that are less important to the tornado maintenance process. Additionally, hail in some storms may have fallen far from the tornado such that its impacts were not directly felt by the tornado or RFD outflow region. It may be that the observed relationships in past work imply a connection between hail production control parameters and the tornadogenesis process, but the lack of hypothesized behaviors in past studies and the complicated multistep process leading to hail development may indicate that it is not a skillful indicator of tornado maintenance.

Decreases in Z_{DR}–K_{DP} separation orientation angle in the time leading up to dissipation are consistent with our hypothesis. Loeffler et al. (2020) hypothesized that as the alignment between the separation vector and storm motion vector became more parallel, more negatively buoyant air is introduced into the updraft region. Although most cases do exhibit a large deviation from 90° (i.e., the two vectors become more aligned) at volume D, large deviations are not exclusive to the dissipation volume and the signal is not as clear as was found with a much larger sample size in Loeffler et al. (2020) and

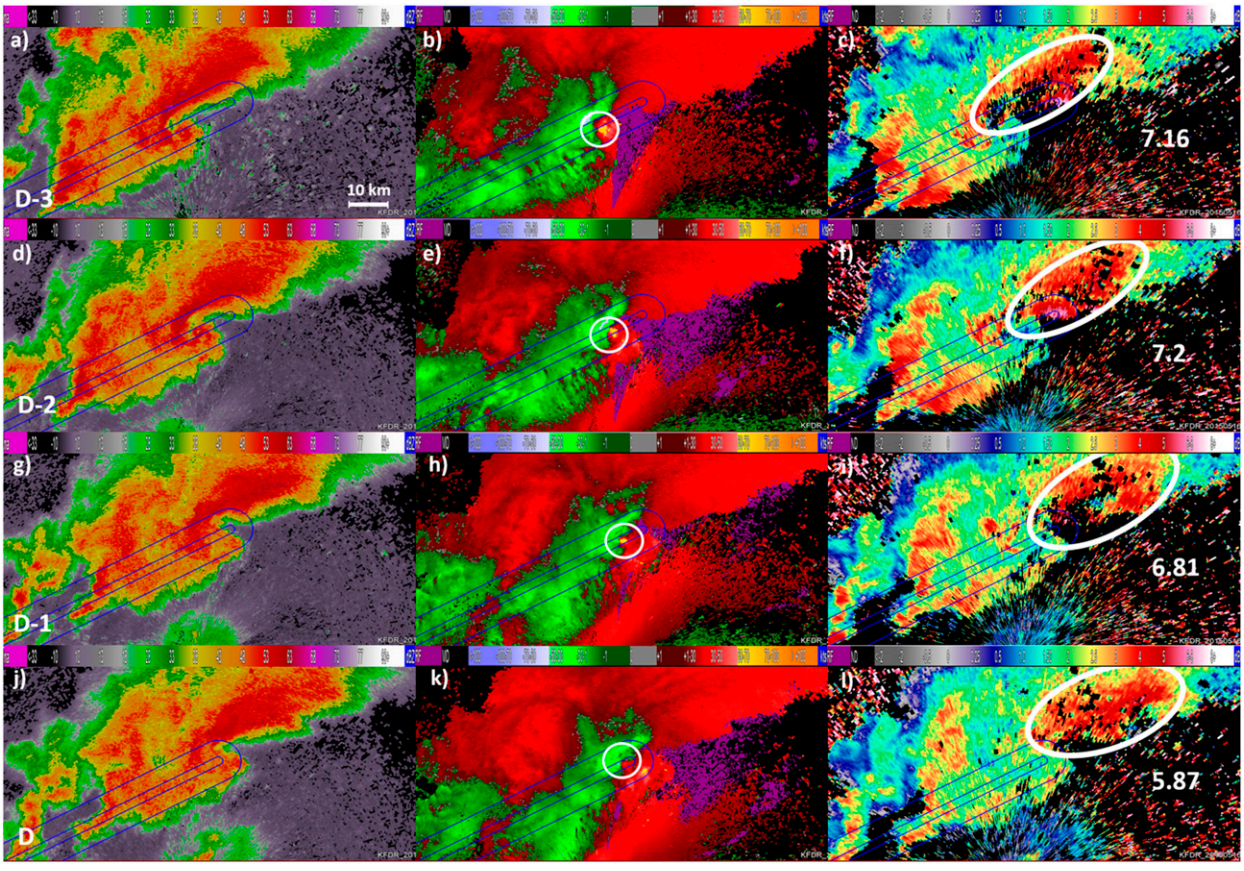

FIG. 12. PPIs displayed in WDSS-II showing the progression of (a),(d),(g),(j) Z_H; (b),(e),(h),(k) radial velocity; and (c),(f),(i),(l) Z_{DR} for 16 May 2015 case at four times: 2329:12, 2334:59, 2340:20, and 2345:34 UTC. Small white circles in (b), (e), (h), and (k) denote the TVS, and larger white ellipses in (c), (f), (i), and (l) mark the Z_{DR} arc. The volume relative to dissipation is indicated in white text in (a), (d), (g), and (j), whereas the Z_{DR} arc's maximum magnitude (dB) is shown in white text in (c), (f), (i), and (l). The blue oval marks the approximate tornado path.

Homeyer et al. (2020). It is possible that this alignment of the separation vector perpendicular to the storm motion vector is a more important precursor for tornadogenesis, but orientation becomes less important for an ongoing tornado owing to the indirect nature of the processes that govern size sorting and tornado maintenance (i.e., a reduction in SRH by itself may not lead to tornado dissipation).

Overall, increases in hook echo K_{DP}, decreases in Z_{DR} arc magnitude, and decreases in Z_{DR}–K_{DP} vector orientation all have some predictive power of tornado dissipation, though we did not specifically test the hypothesized causes of the signature's connection to dissipation. However, given that they are all observed at other times in the tornado life cycle, sometimes frequently, we do not recommend forecasters use their appearance in isolation to confidently assess that a tornado life cycle is ending. Rather, one of the most important results from FK19 is the frequency with which *multiple* TVS dissipation behaviors occur simultaneously almost exclusively near dissipation rather than at earlier times in tornado life cycles. For this study, we combined the storm-scale polarimetric signatures which showed the most promise (hook echo median K_{DP}, Z_{DR} arc, and Z_{DR}–K_{DP} separation orientation angle) with the TVS behaviors from FK19 for the final three volumes (Fig. 15a). The likelihood of observing three or more dissipation behaviors in the same volume increases leading up to tornado dissipation; 23/28 cases display at least three simultaneous behaviors in volume *D* (Fig. 15b). Additionally, the only occurrence of all six observed dissipation behaviors happening simultaneously occurs at volume *D*. However, even this combined signal is not as strong as the combined TVS behavior signal (see Fig. 14 in FK19), likely owing to the storm-scale (and therefore, *indirect*) nature of our polarimetric signatures. The TVS signatures studied in FK19 likely reflect processes *directly* influencing the health of the tornado, resulting in a clearer signal. Therefore, owing to ease of TVS identification, and the stronger dissipation signals, *we advise forecasters at this time to primarily track TVS intensity and TVS location within the storm to inform tornado maintenance health as discussed in* FK19*, while being aware that observed changes in the three aforementioned polarimetric signals may provide additional support for impending tornado dissipation*. This is, of course, in addition to existing tools and techniques

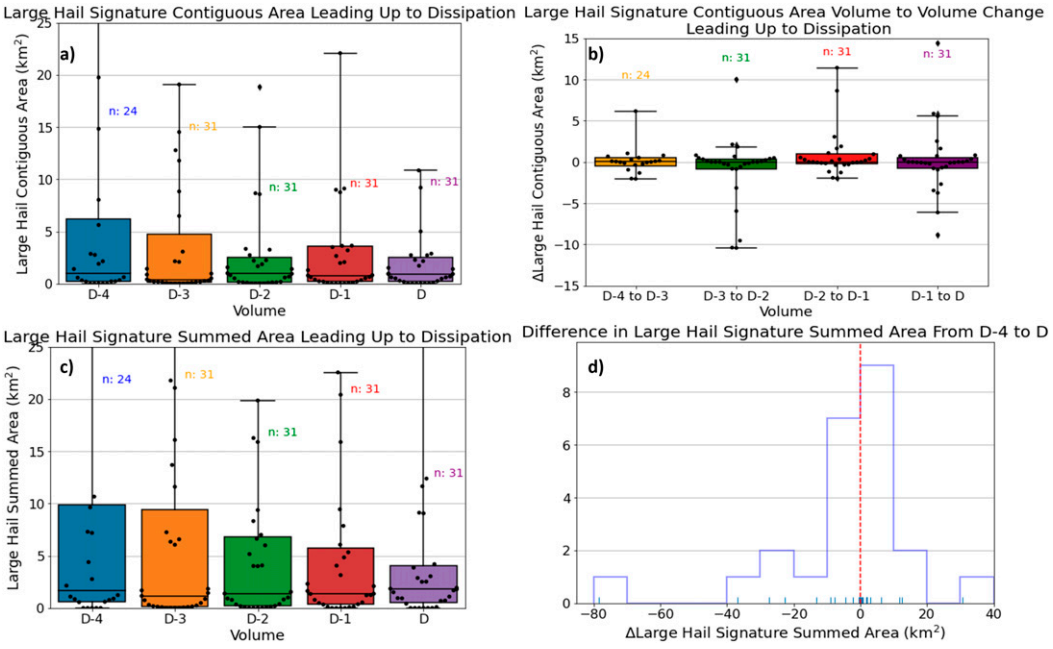

FIG. 13. (a) As in Fig. 6a, but for the large hail signature's contiguous area (km^2); (b) as in Fig. 6b, but for the large hail signature's contiguous area; (c) as in Fig. 6a, but for the large hail signature's summed area (km^2); and (d) as in Fig. 6c, but for the large hail signature's summed area. Some outliers were omitted in (a) and (c) for readability.

to monitor storm-scale evolution that may be less supportive for tornadoes like unfavorable near-storm environments (e.g., lower LCLs, weakening low-level shear) and output from mesoanalyses, high resolution models (e.g., the HRRR), and newer approaches like "Warn-On Forecast."

Some suggestions for additional future work include investigating the origins of K_{DP} and N_T increases within the hook by analyzing several height levels above 500 m. To attain the temporal resolution necessary to identify these origins, mobile radar data with volume scan times much faster than that of the WSR-88D network of radars are required (e.g., McKeown et al. 2020). Increased vertical and temporal resolution should allow these signals to be tracked throughout the storm to highlight the relevant processes responsible for this signal. However, McKeown et al. (2020) did find some high-frequency oscillatory behavior in hook echo behaviors when using rapid-scan data which could be masked when analyzing 4–6-min volume scans, and thus complicate use and interpretation of promising signals. Further, it is unclear if the observed increases occur over the entire hook echo region or if certain areas within the hook are more likely to see increases. Therefore, breaking the hook echo down into smaller regions (similar to French et al. 2015) and examining the trends in Z_{DR}, K_{DP}, D_0, and N_T could further illuminate the important processes responsible for these trends.

The evolution of Z_{DR} columns projected onto constant-altitude plan position indicators (CAPPIs) could produce a stronger signal than the one observed in this study. Owing to the tilting nature of updrafts coupled with the radar geometry at high elevation angles, the output from our Z_{DR} column algorithm at one elevation angle often was observed to span over 1.5 km in height. Even when the median height of the column is ~1 km above the environmental 0°C level, portions of the column output may be within or beneath the environmental 0°C level, as well as over 1.5 km above the environmental 0°C level. CAPPIs allow for the examination of this column at a constant altitude to mitigate the contamination by gates within/below the freezing level. Also, based on the work of Trapp et al. (2017) and Marion et al. (2019), it may be prudent to compare satellite derived overshooting top areas to the observed Z_{DR} column areas to establish a relationship between the two; this could further elucidate the relationship between tornado maintenance and updraft width/area.

In this study, we were unable to investigate any hypothesized environmental controls of signatures and behaviors given the small time windows involved (~20 min between $D - 4$ and D) and the lack of environmental data near storms at sufficient temporal resolution (i.e., at the temporal scale of the WSR-88D, ~300 s). More work into uncovering the relationships, for example, among the Z_{DR} arc maximum magnitude, Z_{DR}–K_{DP} separation orientation, and SR winds and SRH may bolster the results from this study. Until then, it is difficult to prove that the actual relationship between a decreasing Z_{DR} arc maximum magnitude (or increasing orientation angle) and tornado maintenance is lowering SRH. Integrative modeling studies similar to Marquis et al. (2012) may be required to further verify the mechanisms responsible for joint behaviors and their environmental controls.

We view this study coupled with FK19 as a first step to developing radar-based approaches to nowcasting tornado

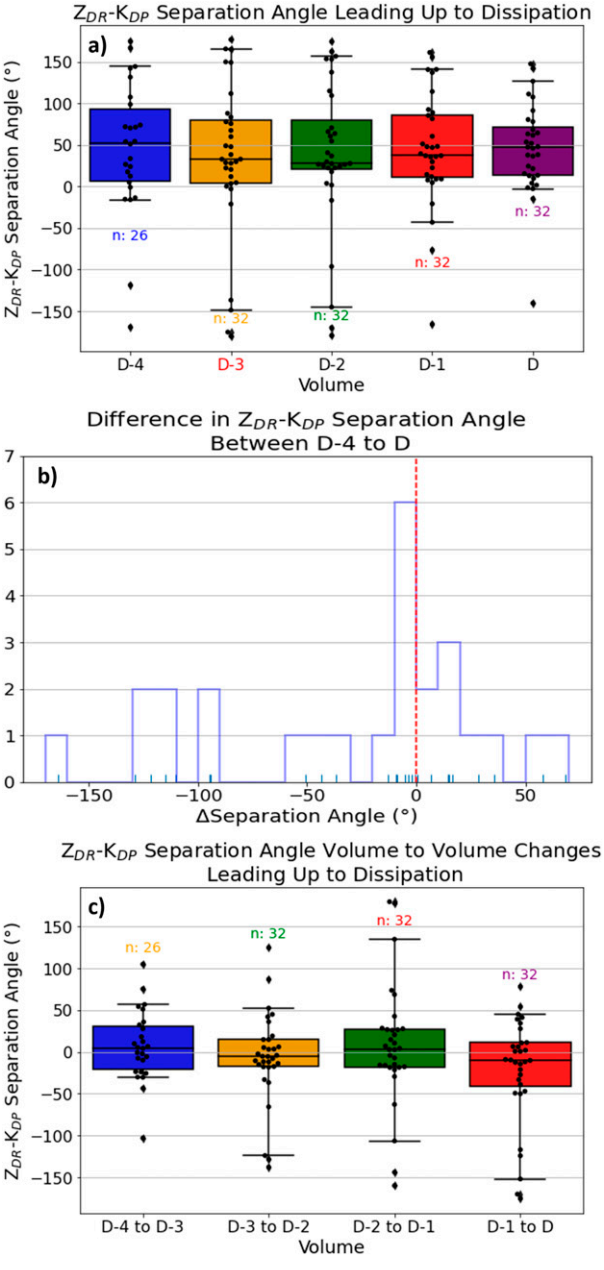

FIG. 14. (a) As in Fig. 6a, but for the Z_{DR}–K_{DP} separation angle (°); (b) as in Fig. 6b, but for Z_{DR}–K_{DP} separation angle; and (c) as in Fig. 6c, but for Z_{DR}–K_{DP} separation angle.

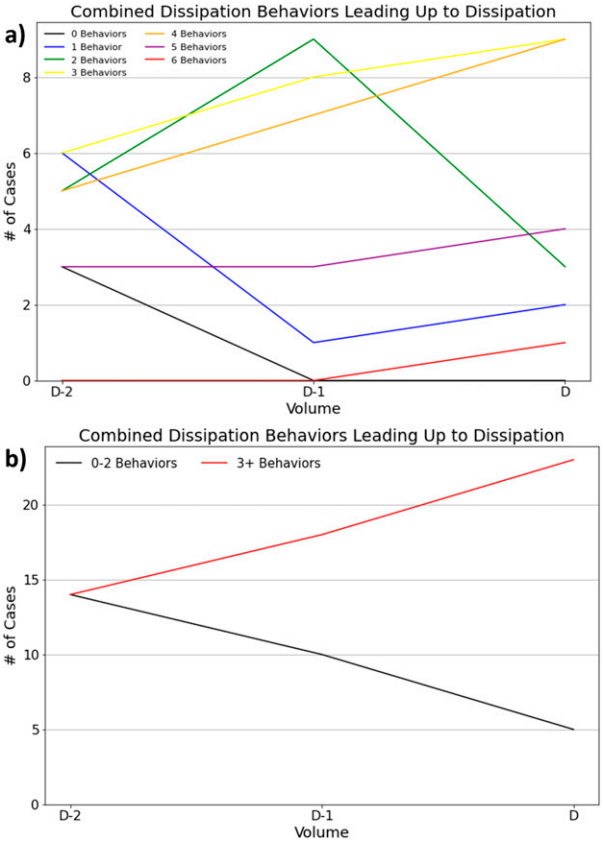

FIG. 15. Plot of the number of cases that displayed (a) 0 (black), 1 (blue), 2 (green), 3 (yellow), 4 (orange), 5 (purple), and 6 (red) behaviors, and (b) 0–2 (black) simultaneous behaviors and 3 or more (red) simultaneous behaviors from volume $D - 2$ leading up to the dissipation volume D.

dissipation. Accurately determining the time of a tornado's demise is an important step in lowering FARs for tornado warnings. Increased confidence that a storm will not reproduce a tornado can reduce the number of subsequent warnings issued on a storm. This helps lessen the number of erroneous warnings and increases public confidence in forecasters. To lessen the workload for forecasters, algorithms should be developed to identify the signatures that showed some promise within this study and FK19. Utilizing machine learning algorithms (e.g., Lagerquist et al. 2020) could potentially aid in this process and lighten the ever-increasing burden on forecasters even more so, though it is likely that a first step will be diagnostic algorithms. One reviewer suggested a weighted algorithm where the previously identified TVS behaviors have a larger weight than the polarimetric signatures investigated within this study. Though diagnostic algorithms still leave some work for the forecaster, it may be best to develop them from this standpoint rather than trying to completely automate the process as the signals are not always unambiguous. Additionally, since each signature examined within this study is representative of processes indirectly related to the tornado, a forecaster still needs to consult and monitor other quantities measured by the radar and other observing systems to get an understanding of the full storm environment.

Acknowledgments. This work was supported by NSF Grants AGS-1748177 (French) and AGS-1748191 (Kingfield). The authors thank Jeffrey Snyder (NOAA/NSSL) for providing the DSD data, and to Brian Colle and Edmund Chang (Stony Brook University) for being on the first

author's M.S. thesis committee and providing help and insight throughout the project.

Data availability statement. The data used in this study, radar data from the WSR-88D and tornado information from *Storm Events*, are freely available from the National Centers for Environmental Information (ncdc.noaa.gov). The output of algorithms and edited case data, including many cases that were not used for various reason summarized in the text, and the resulting files are quite large. Please contact the corresponding author for data access and information about how they can be viewed in WDSS-II.

REFERENCES

Bluestein, H. B., W.-C. Lee, M. Bell, C. C. Weiss, and A. L. Pazmany, 2003: Mobile Doppler radar observations of a tornado in a supercell near Bassett, Nebraska, on 5 June 1999. Part II: Tornado-vortex structure. *Mon. Wea. Rev.*, **131**, 2968–2984, https://doi.org/10.1175/1520-0493(2003)131<2968:MDROOA>2.0.CO;2.

Brandes, E. A., 1977: Gust front evolution and tornado genesis as viewed by Doppler radar. *J. Appl. Meteor.*, **16**, 333–338, https://doi.org/10.1175/1520-0450(1977)016<0333:GFEATG>2.0.CO;2.

Bringi, V. N., and V. Chandrasekar, 2001: *Polarimetric Doppler Weather Radar: Principles and Applications*. Cambridge University Press, 636 pp.

Bunkers, M. J., B. A. Klimowski, J. W. Zeitler, R. L. Thompson, and M. L. Weisman, 2000: Predicting supercell motion using a new hodograph technique. *Wea. Forecasting*, **15**, 61–79, https://doi.org/10.1175/1520-0434(2000)015<0061:PSMUAN>2.0.CO;2.

Cao, Q., G. Zhang, E. Brandes, T. Schuur, A. Ryzhkov, and K. Ikeda, 2008: Analysis of video disdrometer and polarimetric radar data to characterize rain microphysics in Oklahoma. *J. Appl. Meteor. Climatol.*, **47**, 2238–2255, https://doi.org/10.1175/2008JAMC1732.1.

Changnon, S. A., 2009: Tornado losses in the United States. *Nat. Hazards Rev.*, **10**, 145–150, https://doi.org/10.1061/(ASCE)1527-6988(2009)10:4(145).

Dawson, D. T., E. R. Mansell, Y. Jung, L. J. Wicker, M. R. Kumjian, and M. Xue, 2014: Low-level Z_{DR} signatures in supercell forward flanks: The role of size sorting and melting of hail. *J. Atmos. Sci.*, **71**, 276–299, https://doi.org/10.1175/JAS-D-13-0118.1.

——, ——, and M. R. Kumjian, 2015: Does wind shear cause hydrometeor size sorting? *J. Atmos. Sci.*, **72**, 340–348, https://doi.org/10.1175/JAS-D-14-0084.1.

Dennis, E. J., and M. R. Kumjian, 2017: The impact of vertical wind shear on hail growth in simulated supercells. *J. Atmos. Sci.*, **74**, 641–663, https://doi.org/10.1175/JAS-D-16-0066.1.

Dowell, D. C., and H. B. Bluestein, 2002a: The 8 June 1995 McLean, Texas, storm. Part I: Observations of cyclic tornadogenesis. *Mon. Wea. Rev.*, **130**, 2626–2648, https://doi.org/10.1175/1520-0493(2002)130<2626:TJMTSP>2.0.CO;2.

——, and ——, 2002b: The 8 June 1995 McLean, Texas, storm. Part II: Cyclic tornado formation, maintenance, and dissipation. *Mon. Wea. Rev.*, **130**, 2649–2670, https://doi.org/10.1175/1520-0493(2002)130<2649:TJMTSP>2.0.CO;2.

French, M. M., and D. M. Kingfield, 2019: Dissipation characteristics of tornadic vortex signatures associated with long-duration tornadoes. *J. Appl. Meteor. Climatol.*, **58**, 317–339, https://doi.org/10.1175/JAMC-D-18-0187.1.

——, H. B. Bluestein, I. PopStefanija, C. Baldi, and R. T. Bluth. 2013: Reexamining the vertical development of tornadic vortex signature in supercells. *Mon. Wea. Rev.*, **141**, 4576–4601, https://doi.org/10.1175/MWR-D-12-00315.1.

——, ——, ——, ——, and ——. 2014: Mobile, phased-array, Doppler radar observations of tornadoes at X band. *Mon. Wea. Rev.*, **142**, 1010–1036, https://doi.org/10.1175/MWR-D-13-00101.1.

——, W. Burgess, E. R. Mansell, and L. J. Wicker, 2015: Bulk hook echo raindrop sizes retrieved using mobile, polarimetric Doppler radar observations. *J. Appl. Meteor. Climatol.*, **54**, 423–450, https://doi.org/10.1175/JAMC-D-14-0171.1.

Grzych, M. L., B. D. Lee, and C. A. Finley, 2007: Thermodynamic analysis of supercell rear-flank downdrafts from project ANSWERS. *Mon. Wea. Rev.*, **135**, 240–246, https://doi.org/10.1175/MWR3288.1.

Heinselman, P. L., and A. V. Ryzhkov, 2006: Validation of polarimetric hail detection. *Wea. Forecasting*, **21**, 839–850, https://doi.org/10.1175/WAF956.1.

Hirth, B. D., J. L. Schroeder, and C. C. Weiss, 2008: Surface analysis of the rear-flank downdraft outflow in two tornadic supercells. *Mon. Wea. Rev.*, **136**, 2344–2363, https://doi.org/10.1175/2007MWR2285.1.

Homeyer, C. R., T. N. Sandmæl, C. K. Potvin, and A. M. Murphy, 2020: Distinguishing characteristics of tornadic and non-tornadic supercell storms from composite mean analyses of radar observations. *Mon. Wea. Rev.*, **148**, 5015–5040, https://doi.org/10.1175/MWR-D-20-0136.1.

Houser, J. L., H. B. Bluestein, and J. C. Snyder, 2015: Rapid-scan, polarimetric, Doppler radar observations of tornadogenesis and tornado dissipation in a tornadic supercell: The El Reno, Oklahoma, storm of 24 May 2011. *Mon. Wea. Rev.*, **143**, 2685–2710, https://doi.org/10.1175/MWR-D-14-00253.1.

Illingworth, A. J., J. W. F. Goddard, and S. M. Cherry, 1987: Polarization radar studies of precipitation development in convective storms. *Quart. J. Roy. Meteor. Soc.*, **113**, 469–489, https://doi.org/10.1002/qj.49711347604.

Kingfield, D. M., and J. C. Picca, 2018: Development of an operational convective nowcasting algorithm using raindrop size sorting information from polarimetric radar data. *Wea. Forecasting*, **33**, 1477–1495, https://doi.org/10.1175/WAF-D-18-0025.1.

Kirkpatrick, C., E. W. McCaul Jr., and C. Cohen, 2009: Variability of updraft and downdraft characteristics in a large parameter space study of convective storms. *Mon. Wea. Rev.*, **137**, 1550–1561, https://doi.org/10.1175/2008MWR2703.1.

Kosiba, K., J. Wurman, Y. Richardson, P. Markowski, P. Robinson, and J. Marquis, 2013: Genesis of the Goshen County, Wyoming, tornado on 5 June 2009 during VORTEX2. *Mon. Wea. Rev.*, **141**, 1157–1181, https://doi.org/10.1175/MWR-D-12-00056.1.

Kumjian, M. R., 2011: Precipitation properties of supercell hook echoes. *Electron. J. Severe Storms Meteor.*, **6** (5), https://ejssm.org/archives/2011/vol-6-5-2011/.

——, 2013a: Principles and applications of dual-polarization weather radar. Part I: Description of the polarimetric radar variables. *J. Oper. Meteor.*, **1**, 226–242, https://doi.org/10.15191/nwajom.2013.0119.

——, 2013b: Principles and applications of dual-polarization weather radar. Part II: Warm- and cold-season applications. *J. Oper. Meteor.*, **1**, 243–264, https://doi.org/10.15191/nwajom.2013.0120.

——, 2013c: Principles and applications of dual-polarization weather radar. Part III: Artifacts. *J. Oper. Meteor.*, **1**, 265–274, https://doi.org/10.15191/nwajom.2013.0121.

——, and A. V. Ryzhkov, 2008a: Polarimetric signatures in supercell thunderstorms. *J. Appl. Meteor. Climatol.*, **47**, 1940–1961, https://doi.org/10.1175/2007JAMC1874.1.

——, and ——, 2008b: Microphysical differences between tornadic and nontornadic supercell rear-flank downdrafts revealed by dual-polarization radar measurements. Preprints, *24th Conf. on Severe Local Storms*, Savannah, GA, Amer. Meteor. Soc., 3B.4, https://ams.confex.com/ams/pdfpapers/141912.pdf.

——, and ——, 2009: Storm-relative helicity revealed from polarimetric radar measurements. *J. Atmos. Sci.*, **66**, 667–685, https://doi.org/10.1175/2008JAS2815.1.

——, and K. Lombardo, 2020: A hail growth trajectory model for exploring the environmental controls on hail size: Model physics and idealized tests. *J. Atmos. Sci.*, **77**, 2765–2791, https://doi.org/10.1175/JAS-D-20-0016.1.

——, A. P. Khain, N. Benmoshe, E. Ilotoviz, A. V. Ryzhkov, and V. T. J. Phillips, 2014: The anatomy and physics of Z_{DR} columns: Investigating a polarimetric radar signature with a spectral bin microphysical model. *J. Appl. Meteor. Climatol.*, **53**, 1820–1843, https://doi.org/10.1175/JAMC-D-13-0354.1.

Kuster, C. M., J. C. Snyder, T. J. Schuur, T. T. Lindley, P. L. Heinselman, J. C. Furtado, J. W. Brogden, and R. Toomey, 2019: Rapid-update radar observations of Z_{DR} column depth and its use in the warning decision process. *Wea. Forecasting*, **34**, 1173–1188, https://doi.org/10.1175/WAF-D-19-0024.1.

Lagerquist, R., A. McGovern, C. R. Homeyer, D. J. Gagne, and T. Smith, 2020: Deep learning on three-dimensional multiscale data for next-hour tornado prediction. *Mon. Wea. Rev.*, **148**, 2837–2861, https://doi.org/10.1175/MWR-D-19-0372.1.

Lakshmanan, V., T. Smith, G. Stumpf, and K. Hondl, 2007: The Warning Decision Support System–Integrated Information. *Wea. Forecasting*, **22**, 596–612, https://doi.org/10.1175/WAF1009.1.

Lee, B. D., C. A. Finley, and C. D. Karstens, 2012: The Bowdle, South Dakota, cyclic tornadic supercell of 22 May 2010: Surface analysis of rear-flank downdraft evolution and multiple internal surges. *Mon. Wea. Rev.*, **140**, 3419–3441, https://doi.org/10.1175/MWR-D-11-00351.1.

Loeffler, S. D., and M. R. Kumjian, 2018: Quantifying the separation of enhanced Z_{DR} and K_{DP} regions in nonsupercell tornadic storms. *Wea. Forecasting*, **33**, 1143–1157, https://doi.org/10.1175/WAF-D-18-0011.1.

——, and ——, 2020: Idealized model simulations to determine impacts of storm-relative winds on differential reflectivity and specific differential phase fields. *J. Geophys. Res. Atmos.*, **125**, e2020JD033870, https://doi.org/10.1029/2020JD033870.

——, ——, M. Jurewicz, and M. M. French, 2020: Differentiating between tornadic and nontornadic supercells using polarimetric radar signatures of hydrometeor size sorting. *Geophys. Res. Lett.*, **47**, e2020GL088242, https://doi.org/10.1029/2020GL088242.

Marion, G. R., R. J. Trapp, and S. W. Nesbitt, 2019: Using overshooting top area to discriminate potential for large, intense tornadoes. *Geophys. Res. Lett.*, **46**, 12th 520–12th&526, https://doi.org/10.1029/2019GL084099.

Markowski, P. M., and Y. Richardson, 2014: What we know and don't know about tornado formation. *Phys. Today*, **67**, 25–31, https://doi.org/10.1063/PT.3.2514.

——, J. M. Straka, and E. N. Rasmussen, 2002: Direct surface thermodynamic observations within the rear-flank downdrafts of nontornadic and tornadic supercells. *Mon. Wea. Rev.*, **130**, 1692–1721, https://doi.org/10.1175/1520-0493(2002)130<1692:DSTOWT>2.0.CO;2.

——, Y. Richardson, J. Marquis, J. Wurman, K. Kosiba, P. Robinson, E. Rasmussen, and D. Dowell, 2012: The pretornadic phase of the Goshen County, Wyoming, supercell of 5 June 2009 intercepted by VORTEX2. Part II: Intensification of low-level rotation. *Mon. Wea. Rev.*, **140**, 2916–2938, https://doi.org/10.1175/MWR-D-11-00337.1.

——, T. P. Hatlee, and Y. P. Richardson, 2018: Tornadogenesis in the 12 May 2010 supercell thunderstorm intercepted by VORTEX2 near Clinton, Oklahoma. *Mon. Wea. Rev.*, **146**, 3623–3650, https://doi.org/10.1175/MWR-D-18-0196.1.

Marquis, J., Y. Richardson, P. Markowski, D. Dowell, and J. Wurman, 2012: Tornado maintenance investigated with high-resolution dual-Doppler and EnKF analysis. *Mon. Wea. Rev.*, **140**, 3–27, https://doi.org/10.1175/MWR-D-11-00025.1.

McKeown, K. E., M. M. French, K. S. Tuftedal, H. B. Bluestein, D. W. Reif, and Z. B. Wienhoff, 2020: Rapid-scan and polarimetric radar observations of the dissipation of a violent tornado on 9 May 2016 near Sulphur, Oklahoma. *Mon. Wea. Rev.*, **148**, 3951–3971, https://doi.org/10.1175/MWR-D-20-0033.1.

Peters, J. M., C. J. Nowotarski, and H. Morrison, 2019: The role of vertical wind shear in modulating maximum supercell updraft velocities. *J. Atmos. Sci.*, **76**, 3169–3189, https://doi.org/10.1175/JAS-D-19-0096.1.

Pratt, J., 1959: Remarks on zeros and ties in the Wilcoxon signed rank procedures. *J. Amer. Stat. Assoc.*, **54**, 655–667, https://doi.org/10.1080/01621459.1959.10501526.

Reimel, K. J., and M. R. Kumjian, 2021: Evaluation of K_{DP} estimation algorithm performance in rain using a known-truth framework. *J. Atmos. Oceanic Technol.*, **38**, 587–605, https://doi.org/10.1175/JTECH-D-20-0060.1.

Richardson, L. M., W. D. Zittel, R. R. Lee, V. M. Melnikov, R. L. Ice, and J. G. Cunningham, 2017: Bragg scatter detection by the WSR-88D. Part II: Assessment of Z_{DR} bias estimation. *J. Atmos. Oceanic Technol.*, **34**, 479–493, https://doi.org/10.1175/JTECH-D-16-0031.1.

Romine, G. S., D. W. Burgess, and R. B. Wilhelmson, 2008: A dual-polarization-radar-based assessment of the 8 May 2003 Oklahoma City area tornadic supercell. *Mon. Wea. Rev.*, **136**, 2849–2870, https://doi.org/10.1175/2008MWR2330.1.

Ryzhkov, A. V., M. Kumjian, S. Ganson, and A. Khain, 2013: Polarimetric radar characteristics of melting hail. Part I: Theoretical simulations using spectral microphysical modeling. *J. Appl. Meteor. Climatol.*, **52**, 2849–2870, https://doi.org/10.1175/JAMC-D-13-073.1.

Snyder, J. C., A. V. Ryzhkov, M. R. Kumjian, A. P. Khain, and J. C. Picca, 2015: A Z_{DR} column detection algorithm to examine convective storm updrafts. *Wea. Forecasting*, **30**, 1819–1844, https://doi.org/10.1175/WAF-D-15-0068.1.

Thompson, R. L., B. T. Smith, J. S. Grams, A. R. Dean, and C. Broyles, 2012: Convective modes for significant severe thunderstorms in the contiguous United States. Part II: Supercell and QLCS tornado environments. *Wea. Forecasting*, **27**, 1136–1154, https://doi.org/10.1175/WAF-D-11-00116.1.

Trapp, R. J., G. R. Marion, and S. W. Nesbitt, 2017: The regulation of tornado intensity by updraft width. *J. Atmos. Sci.*, **74**, 4199–4211, https://doi.org/10.1175/JAS-D-16-0331.1.

Tuftedal, K. S., M. M. French, D. M. Kingfield, and J. C. Snyder, 2021: Observed bulk hook echo drop size distribution evolution in

supercell tornadogenesis and tornadogenesis failure. *Mon. Wea. Rev.*, **149**, 2539–2557, https://doi.org/ 10.1175/MWR-D-20-0353.1.

Van Den Broeke, M. S., 2016: Polarimetric variability of classic supercell storms as a function of environment. *J. Appl. Meteor. Climatol.*, **55**, 1907–1925, https://doi.org/10.1175/JAMC-D-15-0346.1.

——, 2017: Polarimetric radar metrics related to tornado life cycles and intensity in supercell storms. *Mon. Wea. Rev.*, **145**, 3671–3686, https://doi.org/10.1175/MWR-D-16-0453.1.

——, 2020: A preliminary polarimetric radar comparison of pretornadic and nontornadic supercell storms. *Mon. Wea. Rev.*, **148**, 1567–1584, https://doi.org/10.1175/MWR-D-19-0296.1.

Warren, R. A., H. Richter, H. A. Ramsay, S. T. Siems, and M. J. Manton, 2017: Impact of variations in upper-level shear on simulated supercells. *Mon. Wea. Rev.*, **145**, 2659–2681, https://doi.org/10.1175/MWR-D-16-0412.1.

Wilcoxon, F., 1945: Individual comparisons by ranking methods. *Biom. Bull.*, **1**, 80–83, https://doi.org/10.2307/3001968.

Wurman, J., Y. Richardson, C. Alexander, S. Weygandt, and P. Zhang, 2007: Dual-Doppler and single-Doppler analysis of a tornadic storm undergoing mergers and repeated tornadogenesis. *Mon. Wea. Rev.*, **135**, 736–758, https://doi.org/10.1175/MWR3276.1.

——, D. Dowell, Y. Richardson, P. Markowski, E. Rasmussen, D. Burgess, L. Wicker, and H. B. Bluestein, 2012: The Second Verification of the Origins of Rotation in Tornadoes Experiment. *Bull. Amer. Meteor. Soc.*, **93**, 1147–1170, https://doi.org/10.1175/BAMS-D-11-00010.1.